

***Ab initio* tight-binding description of morphology-dependent resonance in a bisphere**

H. Miyazaki*

Department of Applied Physics, Tohoku University, Aramaki, Aoba 08, 980-8579, Japan

Y. Jimba

College of Engineering, Nihon University, Koriyama, Fukushima, 963-8642, Japan

(Received 30 July 1999; revised manuscript received 8 May 2000)

Morphology-dependent resonance (MDR) of the electric field in a bisphere is investigated with respect to the electromagnetic energy stored within the spheres. The energy spectra clearly reveal the fine structure of the bonding and antibonding branches originating from the Mie resonance of a single sphere. The electric field distribution can directly provide information on the formation of the bonding and antibonding states. On the basis of this detailed information, we establish the *ab initio* tight-binding (TB) formalism of the MDR in a bisphere. The single-mode TB model combined with the linearization of the phase shift clarifies the meaning of the overlap integral. It also gives a qualitative explanation of the MDR. By dividing the Mie resonance modes into the relevant modes and the reservoir modes and incorporating the latter perturbationally, it is shown that the double-mode TB model can reproduce the exact numerical results fairly well.

I. INTRODUCTION

The study of the Mie resonance in a single sphere has a long history of research since the work of Mie¹ and Debye.^{2,3} Detailed investigations of its features have been carried out both experimentally and theoretically.^{4,5} On the basis of this research, its study has matured enough to provide us with a wide range of applications such as lasing in a single sphere by using extremely high Q values of the Mie resonance.^{6,7}

The sharp resonance in a single sphere has naturally invoked an interest in the cooperative resonant scattering from a cluster of spheres. This resonance is generally called the morphology-dependent resonance (MDR). Extensive work has also been devoted to clarify the MDR's, mainly focusing on a bisphere.⁸⁻¹³

In analogy to the quantum-mechanical formation of the molecular orbits, it is expected that the interaction between spheres brings about the bonding and antibonding states of the electromagnetic field. These states can be expressed as a linear combination of the Mie resonance states of each sphere. In fact, Fuller has observed numerically that the electromagnetic coupling between spheres causes the narrow Mie resonance to split into distinct, relatively broad peaks and dips in the forward-scattering spectrum of the bisphere.¹² This split is more clearly observed in the recent photoluminescence study of the photonic molecule.¹⁴ The photonic molecule is made from a pair of photonic dots that are coupled by narrow channels. By comparing the emission peak energies with the calculated eigenmode energies, they found that the optical modes in photonic molecules exhibit strong similarities to those of the electronic states in diatomic molecules.

We have also made a photoluminescence study of a bisphere and found that the coupling between spheres causes a split of the degenerate Mie resonance modes.¹⁵ A clear level crossing is observed between the Mie resonance modes by changing the radius of one of the spheres. These results are in good agreement with the numerical results. In addition, a

phenomenological tight-binding model is shown to reproduce the level crossing fairly well. This work opens up a new possibility to describe MDR's by the tight-binding model.

The phenomenological tight-binding model has also been used very recently to reproduce the band structure of two-dimensional (2D) photonic band-gap (PBG) lattices composed of cylinders.¹⁶ The PBG materials are artificially manufactured materials having a periodic dielectric constant. They have attracted considerable interest because of their potentiality to control the electromagnetic states.¹⁷⁻²⁰ Theoretical and experimental researches are now in progress in many areas of pure and applied physics. For example, we have shown recently that the periodically arranged spheres in 2D show huge enhancement of the electric field near the spheres.^{21,22} This enhancement is due to the evanescent field and is experimentally observed by using the scanning near-field optical microscopy (SNOM).²³ However, the research is limited at present to the region of lower-order Mie resonances. The conventional method to describe the propagation of electric fields between spheres encounters serious numerical difficulties in the higher-order resonance region. This limitation also applies to the band-structure calculation. If, as shown by Lidorikis *et al.*,¹⁶ the propagation of electric fields is described by the tight-binding model, one can design the band structure of PBG materials over a wide range of frequency in a handy and highly efficient way.

To establish the tight-binding description of MDR's an accurate knowledge of the resonance positions is indispensable. For this purpose, the original Mie resonance of a single sphere should be as sharp as possible. Lower resonances have broader peaks due to the lower values of Q so that the split, if it exists, would be smeared out. In fact, Fuller's finding of the split in the bisphere is related to the mode of $l=39$.¹² The split of the $l=16$ mode seems not so clear compared with that of $l=39$. Higher values of l inevitably require the enormous increase of the computation time for the evaluation of expansion coefficients of the vector addition theorem.²⁴⁻²⁶ Although efficient recurrence relations for ex-

pansion coefficients were successively found by Bruning and Lo,⁹ Fuller,¹² Mackowski,¹³ and Xu,²⁷ it is still difficult to deal with a higher-order MDR for a general configuration of spheres. However, this difficulty can be greatly relieved in a uniaxial system, i.e., a linear chain of spheres. To obtain the precise information of MDR's, therefore, we concentrate on the simplest system, i.e., a bisphere. Still, this simple system does not lose any essential feature of the MDR's as shown by the work of Fuller.¹²

Another difficulty in the study of MDR's has its origin in the history of research. The MDR's are traditionally investigated from the viewpoint of scattering cross sections. The scattering cross section is usually governed by the lower-order resonances. The higher-order resonance appears as a tiny but very sharp peak or dip in the scattering spectrum. Use of the backward (radar) cross section seems to be promising because higher-order resonances appear as rather intense peaks or dips.⁵ However, even in this case, lower-order resonances still dominate the spectrum.

In this respect, recent photoluminescence studies of MDR's deserve special attention. The photoluminescence intensity is proportional to the field intensity within spheres. The field intensity can be measured by the internal electromagnetic energy. The internal energy is given as a sum of the bilinear product of the expansion coefficients in terms of the vector spherical harmonics. In contrast, the total scattering cross section is linear owing to the optical theorem.³ Therefore, the bilinear dependence of the internal energy is expected to suppress the contribution from lower-order resonances and enables us to observe clearly the split of higher-order Mie resonances. In addition, the internal energy plays a crucial role in lasing because it gives a direct measure of the quality factor Q . Thus, the first goal of our paper is to determine accurately the positions of MDR's by using the internal energy spectra.

We also present the electric field distribution within each sphere.^{12,28} This visualizes the bonding and antibonding states directly. In addition, it would yield salient information on the more efficient excitation of dye molecules within spheres by the incident field. Interpretations of various features of the internal field are based on the analysis of normal modes of the Mie resonance in a single sphere.

Our second goal is to establish the *ab initio* tight-binding formalism of MDR's. So far, all the analyses have phenomenologically introduced the transfer or overlap integrals between spheres. This is in analogy to the tight-binding description of the band structure in insulators and semiconductors.²⁹ Rigorously speaking, however, this analogy does not hold because the Mie resonance states are not bound within the sphere.^{1,3} The electromagnetic field outside the sphere decays as $1/r$ for $r \rightarrow \infty$. This extended behavior does not guarantee the convergence of the overlap integral between the resonance states of the neighboring spheres. Therefore, the key to this problem is a working definition of the overlap integral.

Combined use of the variational principle and the Green's function gives one possibility. The variational method can be extended to the scattering problem via the use of the Green's function.³⁰ The Green's function formalism has already been established by several authors.³¹⁻³³ This approach, however,

does not give us a transparent definition of the overlap integral.

In the present work, instead, we start with an orthodox formulation of the problem based on the vector spherical harmonics expansion and derive a simple and handy tight-binding equation that clarifies the meaning of the overlap integral. In addition, it gives almost all the qualitative explanations of the characteristic features of MDR's in a bisphere. It should be noted that in our approach the overlap integral can be evaluated exactly. In this sense, the present formalism can be called the *ab initio* tight-binding model.

To take a further step toward a quantitative understanding of MDR's we have to deal with the peak broadening, i.e., the energy dissipation. The energy dissipation is observed to increase significantly in a bisphere.¹² This is due to the interaction of the relevant mode (e.g., $l=39$) with the lower dissipative resonance modes of the neighboring sphere. Since the control of the energy dissipation in the multisphere system is of great interest, it is desirable to include the effect of dissipation via lower resonance modes in the tight-binding formalism.

Now, the lower resonance modes are not only dissipative but they have an enormous amount of freedom. This situation reminds us of the reservoir modes in the theory of projection operator for the evolution of the density matrix.³⁴ In the projection operator theory, the whole system is divided into the relevant system and the reservoir, and the reservoir modes are treated perturbationally. In the present paper, therefore, we follow this procedure and take into account the lower resonance modes perturbationally.

This paper is organized as follows: In Sec. II, we describe the bisphere system and derive the basic equation to determine the internal fields. We also give the expressions of the internal energy and scattering cross sections. Section III is devoted to the presentation and interpretation of various features of MDR's such as the dependence of the internal energy on the incidence angle and on the distance between spheres. Some of the MDR peaks are chosen to study the internal field distribution. All the results in Sec. III are obtained by the exact numerical calculation of the basic equation. In Sec. IV, we present the single-mode tight-binding (SMTB) model and discuss qualitatively the various properties of MDR's presented in Sec. III. The SMTB model is extended to the double-mode version in Sec. V to classify each mode into two groups: the relevant mode and the reservoir mode. Then, the reservoir modes are perturbationally incorporated in the double-mode tight-binding (DMTB) model. Various quantities are numerically evaluated and compared with the results presented in Sec. III. Section VI is devoted to further discussion and summary.

II. MODEL AND FORMULATION

Let us consider two nonmagnetic spheres on the z axis at \mathbf{R}_1 and \mathbf{R}_2 separated by a distance d in the vacuum as shown in Fig. 1. Each sphere has a radius a_i and a uniform dielectric constant ε_i . A linearly polarized plane wave impinges upon the spheres with its amplitude \mathbf{E}_0 and wave vector \mathbf{k}_0 . The wave vector \mathbf{k}_0 is parallel to the xz plane and makes an angle θ with the z axis. \mathbf{E}_0 is parallel either to the xz plane (xz polarization) or to the y axis (y polarization).

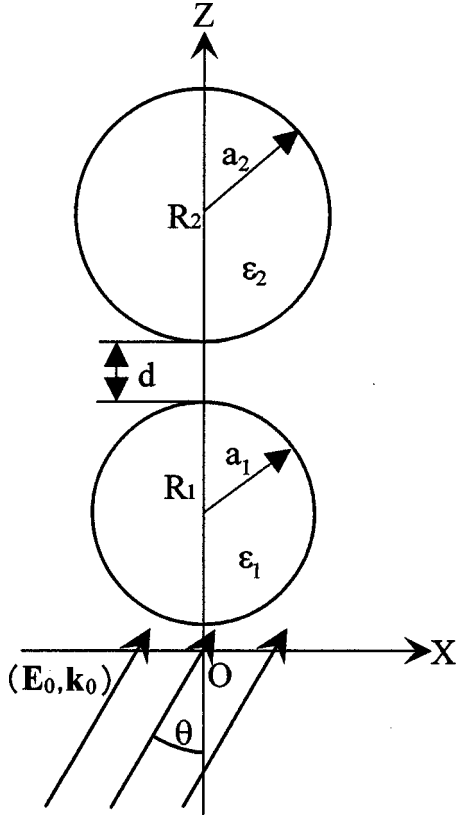


FIG. 1. Bisphere aligned along the z axis. Each sphere has the radius a_i and the dielectric constant ϵ_i . Spheres are centered at \mathbf{R}_1 and \mathbf{R}_2 separated by a distance d . A plane electromagnetic field of amplitude \mathbf{E}_0 is incident with the wave vector \mathbf{k}_0 . \mathbf{k}_0 lies on the xz plane and makes an angle θ with the z axis. \mathbf{E}_0 is either within the xz plane (xz polarization) or parallel to the y axis (y polarization).

The internal, scattered, and incident fields of the i th sphere, \mathbf{E}^w , \mathbf{E}^s , and \mathbf{E}^{inc} , are expanded by the vector spherical harmonics (VSH's) $\{\mathbf{E}_{l,m}^\beta\}$ of the sphere i . By writing $\mathbf{r}_i = \mathbf{r} - \mathbf{R}_i = (r_i, \theta_i, \phi_i)$ in spherical coordinates, they are given as

$$\mathbf{E}^w(\mathbf{r}_i) = \sum_{\beta=M,N} \sum_{l=1}^{\infty} \sum_{m=-l}^l a_{l,m}^{i,\beta} \mathbf{E}_{l,m}^\beta(j_l, k_i r_i, \theta_i, \phi_i), \quad (2.1a)$$

$$\mathbf{E}^s(\mathbf{r}_i) = \sum_{\beta=M,N} \sum_{l=1}^{\infty} \sum_{m=-l}^l b_{l,m}^{i,\beta} \mathbf{E}_{l,m}^\beta(h_l^{(1)}, k_0 r_i, \theta_i, \phi_i), \quad (2.1b)$$

$$\mathbf{E}^{inc}(\mathbf{r}_i) = \sum_{\beta=M,N} \sum_{l=1}^{\infty} \sum_{m=-l}^l c_{l,m}^{i,\beta} \mathbf{E}_{l,m}^\beta(j_l, k_0 r_i, \theta_i, \phi_i). \quad (2.1c)$$

Here, $k_0 = |\mathbf{k}_0|$ and $k_i = \sqrt{\epsilon_i} k_0$ are the wave numbers in the vacuum and within the sphere i , respectively. $\mathbf{E}_{l,m}^\beta(f, k r, \theta, \phi)$ is a VSH of the transverse electric (TE) mode for $\beta=M$ or the transverse magnetic (TM) mode for $\beta=N$.³⁵ The function $f=f(kr)$ is either the spherical Bessel function $j_l(kr)$ or the spherical Hankel function of the first kind $h_l^{(1)}(kr)$. The definition of the VSH's is given in Ap-

pendix A. We also give in Appendix B the explicit expression and symmetry relations of $\{c_{l,m}^{i,\beta}\}$ for the incident plane wave.

The scattered field from one sphere is the additional incident field for the other sphere. To satisfy the boundary condition on the surface of each sphere, therefore, we expand the scattered field from the j th sphere in terms of the VSH's of the i th sphere. This is done by using the following vector addition theorem:

$$\begin{aligned} & \mathbf{E}_{l,m}^\beta(h_l^{(1)}, k_0 r_j, \theta_j, \phi_j) \\ &= \sum_{\gamma=M,N} \sum_{p=1}^{\infty} \sum_{q=-p}^p \mathbf{E}_{p,q}^\gamma(j_p, k_0 r_i, \theta_i, \phi_i) A_{p,q;l,m}^{\gamma,\beta}(k_0, \mathbf{R}^{ji}), \end{aligned} \quad (2.2)$$

where $\mathbf{R}^{ji} = \mathbf{R}_i - \mathbf{R}_j$. The expansion coefficients $A_{p,q;l,m}^{\gamma,\beta}(k_0, \mathbf{R}^{ji})$ are obtained either by a direct evaluation of the Wigner 3- j symbols²⁶ or by the recurrence relation of Mackowski.¹³ They are summarized in Appendix C. In the case of a bisphere along the z axis, the summation over q in Eq. (2.2) is limited to only $q=m$.

Since the present work focuses on the internal field, we derive an equation relating the internal field to the incident plane wave. The boundary condition combined with the vector addition theorem yields the following basic equation for $a_{l,m}^{i,\beta}$:

$$\begin{aligned} & a_i^2 (\cot \delta_l^{i,\beta} - i) \tilde{a}_{l,m}^{i,\beta} - i \sum_{j(\neq i)} \sum_{\gamma=M,N} \sum_{p=1}^{\infty} a_j^2 A_{l,m;p,m}^{\gamma,\beta} \\ & \times (k_0, \mathbf{R}^{ji}) \tilde{a}_{p,m}^{j,\gamma} \\ &= \tilde{c}_{l,m}^{i,\beta}. \end{aligned} \quad (2.3)$$

Here, $\cot \delta_l^{i,\beta}$, $\tilde{a}_{l,m}^{i,\beta}$, and $\tilde{c}_{l,m}^{i,\beta}$ are introduced to symmetrize the equation

$$\begin{aligned} \tilde{a}_{l,m}^{i,\beta} &\equiv >D_l^{i,\beta} a_{l,m}^{i,\beta}, \\ \tilde{c}_{l,m}^{i,\beta} &\equiv -\frac{1}{k_0} c_{l,m}^{i,\beta}, \\ \cot \delta_l^{i,\beta} &\equiv i \left(1 - \frac{<D_l^{i,\beta}}{>D_l^{i,\beta}} \right). \end{aligned} \quad (2.4)$$

The functions $<D_l^{i,\beta}$ and $>D_l^{i,\beta}$ are defined as

$$<D_l^{i,M} = k_i h_l^{(1)}(k_0 a_i) j_l'(k_i a_i) - k_0 h_l^{(1)'}(k_0 a_i) j_l(k_i a_i), \quad (2.5a)$$

$$>D_l^{i,M} = k_i j_l(k_0 a_i) j_l'(k_i a_i) - k_0 j_l'(k_0 a_i) j_l(k_i a_i), \quad (2.5b)$$

$$\begin{aligned} <D_l^{i,N} &= [k_0 \xi_l(k_0 a_i) \psi_l'(k_i a_i) \\ & - k_i \xi_l'(k_0 a_i) \psi_l(k_i a_i)] / (a_i^2 k_0 k_i), \end{aligned} \quad (2.5c)$$

$$\begin{aligned} >D_l^{i,N} &= [k_0 \psi_l(k_0 a_i) \psi_l'(k_i a_i) \\ & - k_i \psi_l'(k_0 a_i) \psi_l(k_i a_i)] / (a_i^2 k_0 k_i), \end{aligned} \quad (2.5d)$$

where $\xi_l(z) = zh_l^{(1)}(z)$, $\psi_l(z) = zj_l(z)$, and the prime denotes the differentiation with respect to the argument. The scattering coefficient $b_{l,m}^{i,\beta}$ is given by

$$b_{l,m}^{i,\beta} = -ik_0 a_i^2 \text{>} D_l^{i,\beta} a_{l,m}^{i,\beta}. \quad (2.6)$$

The quantity $\delta_l^{i,\beta}$ represents the phase shift of the spherical outgoing wave of mode (β, l) from the i th sphere³¹ and plays an important role in the present analysis. To clarify its meaning we consider the case of a single sphere. Then, Eqs. (2.3) and (2.6) yield

$$a_{l,m}^{i,\beta} = -i \frac{c_{l,m}^{i,\beta}}{\text{<} D_l^{i,\beta} k_0 a_i^2}, \quad (2.7a)$$

$$b_{l,m}^{i,\beta} = - \frac{\text{>} D_l^{i,\beta}}{\text{<} D_l^{i,\beta}} c_{l,m}^{i,\beta} = \frac{i}{\cot \delta_l^{i,\beta} - i} c_{l,m}^{i,\beta} = \frac{1}{2} (e^{2i\delta_l^{i,\beta}} - 1) c_{l,m}^{i,\beta}. \quad (2.7b)$$

As seen, $|b_{l,m}^{i,\beta}|$ becomes maximum when $\cot \delta_l^{i,\beta} = 0$. Therefore, $\cot \delta_l^{i,\beta} = 0$ gives the Mie resonance positions of a single sphere. In general, the sharp Mie resonance occurs when $k_0 a_i \leq l + 1/2$ and $l \gg 1$. In this region, j_l shows exponential decay and $h_l^{(1)}$ increases exponentially. For general values of k_0 , therefore, we have $|\text{<} D_l^{i,\beta}| \gg |\text{>} D_l^{i,\beta}|$. At the Mie resonance, however, $\text{>} D_l^{i,\beta} = \text{<} D_l^{i,\beta}$ is satisfied so that $|\text{<} D_l^{i,\beta}|$ reduces significantly. This results in an enormous increase of $a_{l,m}^{i,\beta}$ and gives huge enhancement of the internal field as seen from Eq. (2.7a).

In the present work, we use the internal energy U to find out the positions of MDR's. The expression of U is obtained by integrating the energy density within the bisphere volume region V_1 and V_2 :

$$\begin{aligned} U &= \frac{1}{8\pi} \sum_i \int_{V_i} d\mathbf{r}_i [\varepsilon_i |\mathbf{E}(\mathbf{r}_i)|^2 + \mu_i |\mathbf{H}(\mathbf{r}_i)|^2] \\ &= \frac{1}{8\pi} \sum_{i,\beta} \sum_{l,m} \varepsilon_i |a_{l,m}^{i,\beta}|^2 f_l(k_i a_i). \end{aligned} \quad (2.8)$$

Here, f_l is given by

$$\begin{aligned} f_l(k_i a_i) &= \frac{l(l+1)}{2l+1} [l g_{l+1}(k_i a_i) + (2l+1) g_l(k_i a_i) \\ &\quad + (l+1) g_{l-1}(k_i a_i)], \end{aligned} \quad (2.9)$$

with $g_l(ka)$ defined as

$$\begin{aligned} g_l(ka) &\equiv \int_0^a dr r^2 j_l^2(kr) \\ &= \frac{a^3}{2} \begin{cases} j_l^2(ka) - j_{l-1}(ka) j_{l+1}(ka) & \text{for } l \geq 1, \\ j_0^2(ka) + n_0(ka) j_1(ka) & \text{for } l = 0, \end{cases} \end{aligned} \quad (2.10)$$

where n_0 is the spherical Neumann function of order 0.

Most of the traditional work deals with the far-field behavior, i.e., scattering cross sections. To compare their resonant behavior with that of U we also calculate the total,

forward, and backward (radar) cross sections C_{total} , $C_{forward}$, and $C_{backward}$. C_{total} is given from the optical theorem as

$$C_{total} = - \frac{1}{\pi a_1^2 k_0^2} \sum_{i,\beta} \sum_{l,m} l(l+1) \text{Re}\{b_{l,m}^{i,\beta} (c_{l,m}^{i,\beta})^*\}. \quad (2.11)$$

Note that C_{total} is equal to the extinction coefficient when there is no absorption within the spheres. $C_{forward}$ is defined by

$$C_{forward} = \lim_{r \rightarrow \infty} \frac{4\pi r^2}{\pi a_1^2 |\mathbf{E}_0|^2} |\mathbf{E}(r, \theta, \phi = 0)|^2, \quad (2.12)$$

where \mathbf{E}_0 is the amplitude of the incident plane wave and θ is the incidence angle. $C_{backward}$ is given by Eq. (2.12) with the replacement of $\theta \rightarrow \pi - \theta$. The asymptotic form of the scattering field yields

$$\begin{aligned} C_{forward} &= \frac{4}{k_0^2 a_1^2} \left[\left| \sum_{l,m,i} (-i)^l \exp(i\mathbf{k}_s \cdot \mathbf{R}_i) \right. \right. \\ &\quad \times \left(b_{l,m}^{i,N} \frac{\partial Y_{l,m}}{\partial \theta} + b_{l,m}^{i,M} \frac{m Y_{l,m}}{\sin \theta} \right) \left. \right|^2 + \left| \sum_{l,m,i} (-i)^l \right. \\ &\quad \times \left. \exp(i\mathbf{k}_s \cdot \mathbf{R}_i) \left(b_{l,m}^{i,N} \frac{m Y_{l,m}}{\sin \theta} + b_{l,m}^{i,M} \frac{\partial Y_{l,m}}{\partial \theta} \right) \right|^2 \Big]. \end{aligned} \quad (2.13)$$

Here, $\mathbf{k}_s = k_0 \mathbf{r}' / |\mathbf{r}'|$ and \mathbf{r} is the point of observation. It is commonly recognized that $C_{backward}$ varies more drastically at the Mie resonance than C_{total} or $C_{forward}$.

III. RESULTS OF THE EXACT NUMERICAL CALCULATION

In this section, we give the exact numerical results of MDR's in a bisphere based on Eq. (2.3). To study the MDR in detail we focus on the case of polystyrene spheres with $a_1 = a_2 = 2.5 \mu\text{m}$ and $\varepsilon_1 = \varepsilon_2 = (1.59)^2$. Other cases are denoted wherever necessary. In principle, the Mie resonance is labeled by a set of four indices, β , l , m , and n . The natural number l characterizes the famous ringlike pattern of the electric field along the circumference of the sphere, i.e., whispering gallery (WG). n is also a natural number indexing the radial behavior of the field. The distribution of the electric field along the radial axis becomes broader for higher n . The Mie resonance of mode l has $(2l+1)$ -fold degeneracy. Each degenerate state is labeled by m with $-l \leq m \leq l$. The incident plane wave along the z axis can only excite the modes $m = \pm 1$. In the single sphere, we can always choose the direction of incidence as the z axis. Therefore, the index m is usually omitted. Thus, the WG mode of a single sphere is usually denoted as, e.g., 39TE1 for $\beta = M$ (TE), $l = 39$, and $n = 1$.

A. U and C 's of a single sphere

Before studying MDR's in a bisphere, let us compare the scattering cross sections with the internal energy of a single sphere. Instead of k_0 we use the size parameter $S \equiv k_0 a_1$. In

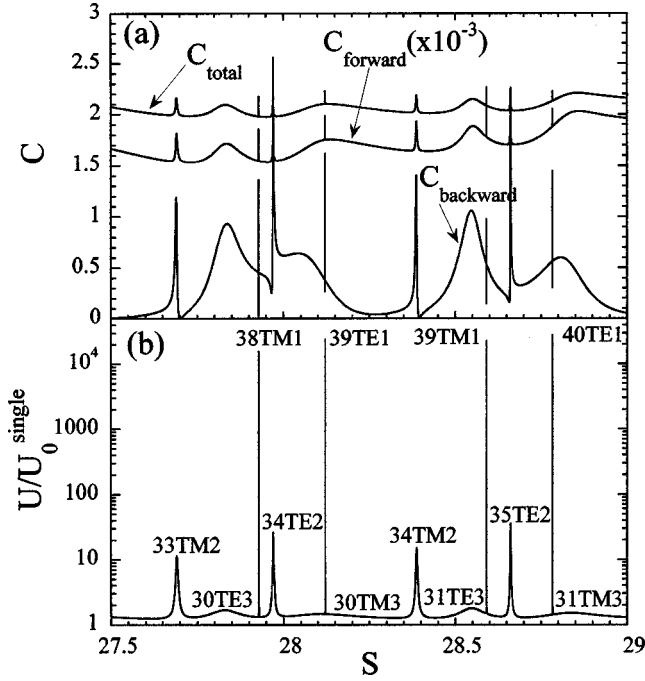


FIG. 2. (a) Scattering cross sections C_{total} , $C_{forward}$, and $C_{backward}$ and (b) internal electromagnetic energy U of a single sphere versus the size parameter $S=k_0a$. The radius and the dielectric constant are chosen as $a=2.5 \mu\text{m}$ and $\epsilon=(1.59)^2$. The scattering cross sections are normalized by the cross-sectional area of the sphere. $C_{forward}$ is multiplied by 10^{-3} for the guide to eyes. The internal energy is also normalized by the vacuum electromagnetic energy within the sphere $U_0^{single}=\frac{1}{3}a_1^3$. Each peak in the energy spectrum is labeled, in principle, by four indices (l,β,m,n) , but m is usually omitted because of the degeneracy. The modal number of each peak in the scattering cross sections can be identified by the corresponding sharp or broad peak in the energy spectrum. Note the linear and logarithmic scales of the vertical axis in (a) and (b).

honor of the work by Fuller,¹² we mainly focus on the range of $27.5 \leq S \leq 29$, which contains the following WG modes: 39TE1 ($S=28.12142$), 39TM1 ($S=28.59165$), 40TE1 ($S=28.78350$), 34TM2 ($S=28.38742$), 35TE2 ($S=28.66183$), 30TM3 ($S=28.10955$), 31TE3 ($S=28.55154$), 31TM3 ($S=28.83720$). All of the spectra in this subsection are calculated with $l \leq l_{max}=60$, which guarantees sufficient numerical convergence for $S \leq 29$.

Figure 2(a) shows the normalized cross sections C_{total} , $C_{forward}$, and $C_{backward}$ for $27.5 \leq S=k_0a_1 \leq 29$. We observe four sharp peaks ($n=1$), four slightly broad peaks ($n=2$), and four broad peaks ($n=3$). As seen from the figure, C_{total} and $C_{forward}$ resemble each other, but $C_{forward}$ is much larger than C_{total} . This means that the total scattering is mostly governed by the strong forward scattering. It is to be noticed that their variations are small, i.e., $\Delta C_{total}/C_{total} \approx 12\%$ and $\Delta C_{forward}/C_{forward} \approx 20\%$. In contrast, $C_{backward}$ shows a large variation. This large variation can be used to identify the position of the Mie resonance. However, the common feature of these three cross sections is that the spectrum is dominated by the lower-order resonances as pointed out in Sec. I.

Figure 2(b) shows the internal energy spectrum U . U is normalized by the vacuum electromagnetic energy within a sphere, $U_0^{single}=\frac{1}{3}a_1^3$. Note the logarithmic scale of the ver-

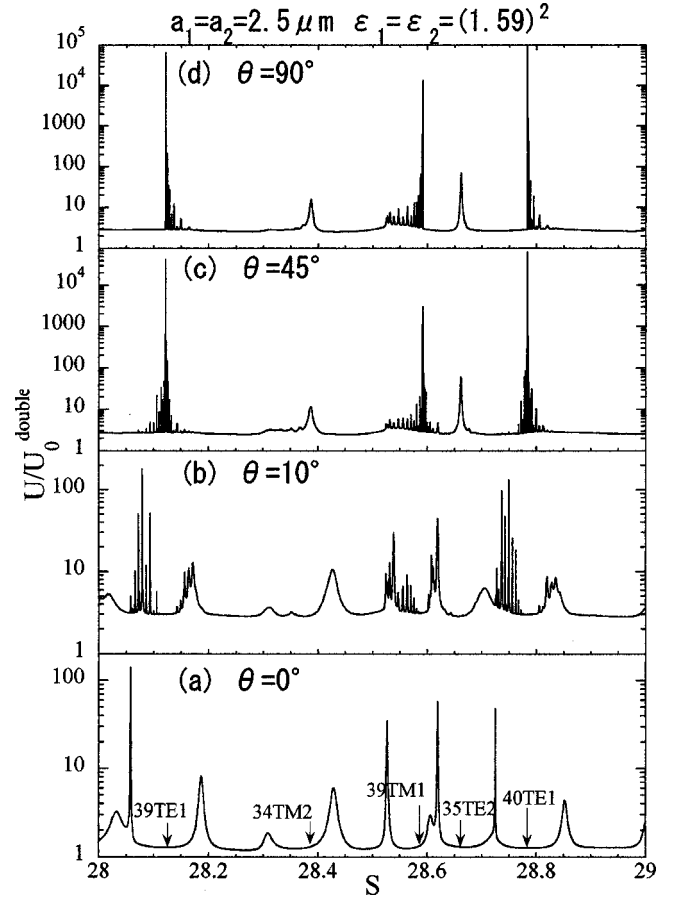


FIG. 3. Internal energy U vs size parameter $S=k_0a_1$ at incidence angle $\theta=0^\circ$ (a), 10° (b), 45° (c) and 90° (d). The polarization is chosen to lie on the xz plane. U is normalized by the vacuum electromagnetic energy within the bisphere $U_0^{double}=2U_0^{single}=\frac{2}{3}a_1^3$. The Mie resonance positions of a single sphere are indicated by the arrows in (a).

tical axis. As seen from the figure, the Mie resonance of smaller n has sharper peak, typical width being $\Delta S \approx 10^{-6}$ for $n=1$. In addition, all the peaks show the Lorentzian line shape. These two features are associated with the quadratic dependence of U on $a_{l,m}^\beta$ in Eq. (2.8). At the Mie resonance, a huge increase of $a_{l,m}^\beta$ occurs due to the decrease of $\langle D_l^\beta \rangle$. Near the resonant size parameter $S_{l,n}^\beta$, $\langle D_l^\beta \rangle$ is linearized as $\langle D_l^\beta \rangle \propto S - S_{l,n}^\beta + i\Delta S_{l,n}^\beta$. This expansion gives the Lorentzian line shape centered at $S=S_{l,n}^\beta$ with full width at half maximum (FWHM) $2\Delta S_{l,n}^\beta$. The comparison between C 's and U in Fig. 2 obviously shows the superiority of U to C 's in the study of Mie resonances.

B. Bispheres in contact

Let us study the case of identical two spheres in contact. Figure 3 shows a series of energy spectra for four cases of incidence angles $\theta=0^\circ$, 10° , 45° , and 90° with the common xz polarization. All the spectra are normalized by the vacuum electromagnetic energy of the bisphere $U_0^{double}=\frac{2}{3}a_1^3$. Numerical convergence of the spectra is achieved for $l \leq l_{max}=59$. Before specifying the characteristic feature of the mode split in bisphere: (1) the interaction be-

tween spheres is limited only between modes of the same m as seen from Eq. (2.3), and (2) no degeneracy is removed between m and $-m$ as shown in Appendix B. Therefore, the total number of peaks originating from a certain l mode is at most $2(l+1)$ in the range $0 \leq |m| \leq l$. These peaks are grouped into the bonding and antibonding branches.

At $\theta=0^\circ$, the incident wave can only excite $m=\pm 1$. Hence, Fig. 3(a) shows the mode split of $(\beta, l, \pm 1, n)$ only. As seen, 39TE1 and 40TE1 modes are almost symmetrically split, but the upper peak is broader than the lower one (note that the broad small peak at $S \cong 28.03$ is the upper peak of mode 34TE2). In contrast, mode 39TM1 shows the asymmetric split with almost the same width. In this respect, it is worth pointing out that the lower peak of mode 35TE2 appears as a small peak just below the upper peak of mode 39TM1. This fact suggests that the asymmetric split of mode 39TM1 is attributed to the interaction with 35TE2. This point will be clarified in Sec. V by the double-mode tight-binding model. As was observed by Fuller, all the peaks are much broadened compared with the peaks of the single sphere in Fig. 2(b). Obviously, this broadening is due to the interaction with more dissipative modes of lower l .

The energy spectrum at $\theta=10^\circ$ in Fig. 3(b) becomes very complicated, showing a lot of spiky or tiny peaks between the upper and lower peaks of $m=\pm 1$. These peaks are due to the presence of $m \neq \pm 1$ components in the incident plane wave though main components are still $m=\pm 1$. The expression of $c_{l,m}^{i,\beta}$ in Appendix B shows that $|c_{l,m}^{i,\beta}|$ decreases with the increasing $|m|$ for small θ . Consequently, the peak of higher $|m|$ is expected to become smaller. As seen in the upper branch of mode 39TE1, the peak intensity decreases as it approaches the Mie resonance of a single sphere. Therefore, the inner peak corresponds to higher $|m|$. Now, the inner peak position means the smaller split. Thus, we conclude that the interaction of mode $|m|$ decreases with increasing $|m|$.

While the spectrum looks complicated, its main feature is still preserved, that is, modes 39TE1 and 40TE1 have upper broad peaks and lower sharp peaks while mode 39TM1 has sharp peaks on both sides. The broad peak near $S=28.7$ is the upper branch of mode 35TE2. Note that the upper branch of mode 39TM1 shows a more complicated line shape than other branches. This is again due to the overlap with the lower branch of mode 35TE2.

The energy spectrum changes drastically when we increase θ to $\theta=45^\circ$. As seen in Fig. 3(c), modes of $n=1$ appear as a dense collection of very sharp peaks around the Mie resonance size parameter $S_{l,1}^\beta$. Peaks of higher n are very similar to those of a single sphere, but they are accompanied with tiny ripples. These features are preserved even at $\theta=85^\circ$ (not shown). At $\theta=90^\circ$, however, one side of the branches of all the $n=1$ modes disappears. We observe in Fig. 3(d) only the upper branch of TE modes and the lower branch of the 39TM1 mode. This probably holds for higher values of n as well, but is not clearly seen because of the large peak width. These characteristic changes of U by the incidence angle θ are also observed for the y polarization incidence except that at $\theta=90^\circ$ the presence of the upper and lower branches of $n=1$ modes is reversed.

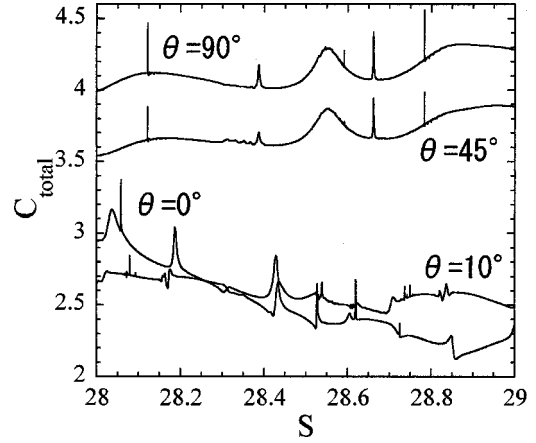


FIG. 4. Total scattering cross section C_{total} in correspondence to the energy spectra in Fig. 3. C_{total} is normalized by the cross-sectional area of a single sphere.

Figure 4 shows C_{total} for the corresponding values of θ in Fig. 3. At $\theta=0^\circ$, the split of $n=1$ modes can be identified by the sharp peaks in the broad background structure. At $\theta=10^\circ$, however, the fine structure due to $n=1$ modes can be hardly recognized because of their small amplitudes. This is also the case for $\theta=45^\circ$ and $\theta=90^\circ$. The spectra consist of sharp peaks, each of which is located at the Mie resonance position $S_{l,n}^\beta$ and is accompanied with very small ripples. The broad peak at $S \cong 28.55$ is identified as mode 31TE3 from Fig. 2(b). We conclude, therefore, that the energy spectrum is more suitable for the study of MDR's in a bisphere than the scattering spectra.

C. Internal field of bisphere in contact

The internal field distribution plays an important role in the analysis of the emission process from the bisphere, because the emission from, say, doped dye molecules is proportional to the field intensity. Detailed knowledge of the internal field distribution gives valuable information to improve the efficiency of lasing in bisphere. It is also intriguing to confirm directly that the lower and upper branches correspond to the bonding and antibonding states of the Mie resonance. In addition, we expect to observe a variety of m -dependent field patterns for off-axis incidence. Some of them would be different from the famous image of WG modes.

In Figs. 5(a) to 5(f), we display the internal field distributions by picking out some of the peaks in the energy spectra of Fig. 3. The incident wave is xz polarized. All the figures give the contour maps of the electric field $|\mathbf{E}(\mathbf{r})|$ over the range of $-a_1 \leq x, y \leq a_1$ and $-a_1 \leq z \leq 3a_1$. The interpretation of the field distribution is based on the analysis of normal modes in a single sphere. Details are described in Appendix D, where special attention is paid to the maxima of the field distribution along the circumference. Results are summarized in Tables I and II.

Figure 5(a) corresponds to the bonding peak of mode 39TE1 at $S=28.05862$ in Fig. 3(a). The famous WG ring-like pattern is seen in each sphere within the yz plane. Note that the electric field is maximum at the contact point of the spheres. This is in contrast to the antibonding peak of mode 39TE1 in Fig. 5(b) at $S=28.18699$, where the electric field

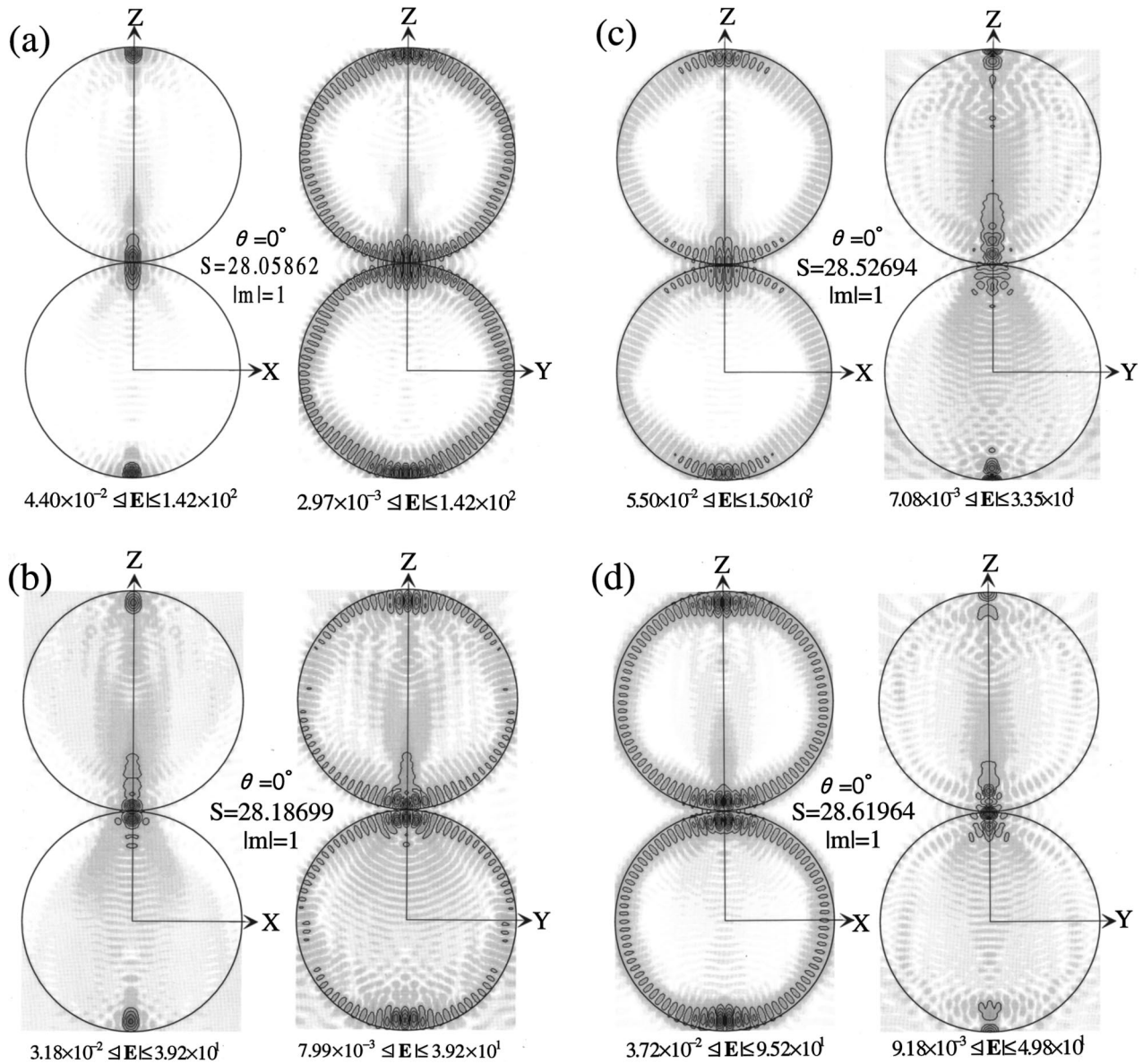


FIG. 5. Distribution of the electric field $|\mathbf{E}|$ within the xz and the yz planes ($-a \leq x, y \leq a$, $-a \leq z \leq 3a$) at some of the MDR peaks of the energy spectra in Fig. 3. (a) and (b) are the bonding and antibonding states of 39TE1 in Fig. 3(a) while (c) and (d) are those of 39TM1. (e) is picked out from the antibonding branch of 39TM1 at $\theta = 10^\circ$ in Fig. 3(b). (f) is from 39TE1 at $\theta = 45^\circ$ in Fig. 3(c). The darker region corresponds to the higher field.

vanishes at the contact point. Thus, the contour map of the internal field indeed can display the bonding and antibonding states of bisphere.

The bonding and antibonding states of mode 39TM1 at $\theta = 0^\circ$ are shown, respectively, in Fig. 5(c) ($S = 28.52694$) and Fig. 5(d) ($S = 28.61964$). While the characteristic ringlike pattern can be seen within the xz plane of the antibonding state in Fig. 5(d), it is not so clear in the bonding state in Fig. 5(c). This reason is unknown at present. An interesting point of Fig. 5(d) is that the contour map within the yz plane seems to imply the bonding state. This reason will be clarified in the next section from the tight-binding model combined with the symmetry properties of normal modes in a single sphere.

Figure 5(e) is the contour map of the peak at $S = 28.61919$ in the antibonding branch of mode 39TM at $\theta = 10^\circ$. It is remarkable that both contour maps show almost

the same ringlike pattern. As explained in Appendix D, this is evidence of even m . We can determine the value of m by referring to Tables I and II. For $\beta = N$, the internal field is dominated by the radial component F_r . From Table I, F_r depends on θ as $P_l^m(\cos \theta)$. From Table II, $|P_l^m(\cos \theta)|$ has $l - m + 1$ maxima in the range of $0 \leq \theta \leq \pi$. Each sphere of Fig. 5(e) has 38 spots along the circumference of the $x > 0$ or $y > 0$ region. This should be equal to $l - m + 1 = 40 - m$. Thus, we conclude $m = 2$. In some cases, it is difficult to identify m from the contour maps within the xz and yz planes. In this case, m can be determined from the contour map within the xy plane because the number of spots within the xy plane is $2m$ from Table I.

Finally, in Fig. 5(f) we show the contour maps of one of the peaks at $S = 28.59165$ in the bonding branch of mode 39TM1 at $\theta = 45^\circ$. It is hard to determine whether it is the bonding or antibonding state because the contact point has

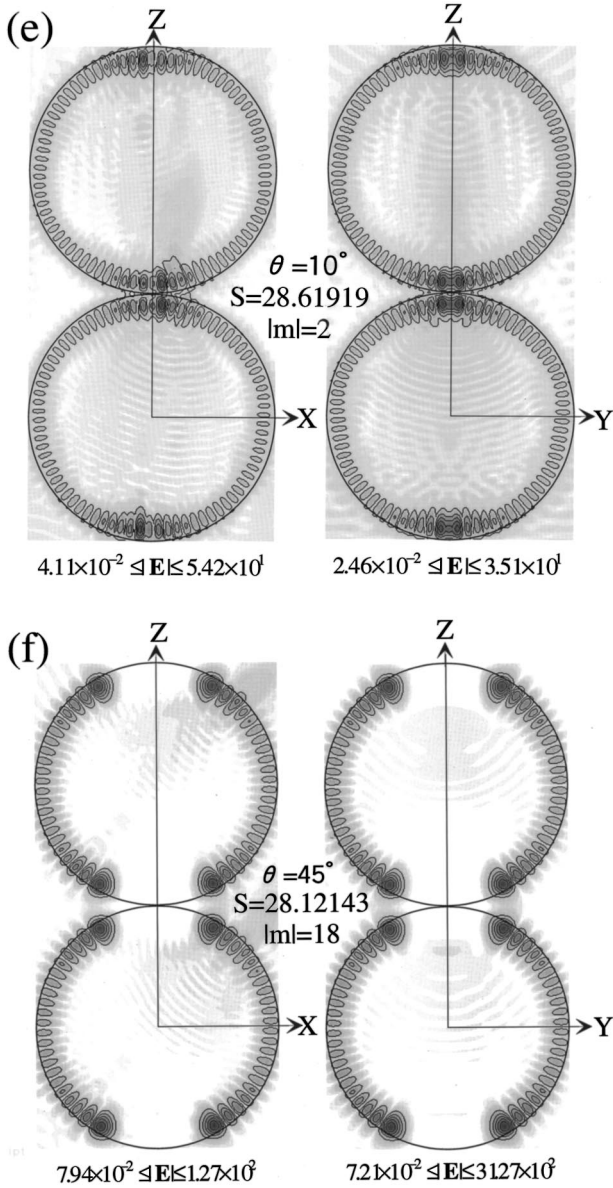


FIG. 5. (Continued).

almost no amplitude. This usually happens for higher values of m . In fact, the number of spots tells us that $m = 18$ in Fig. 5(f). The smaller field intensity at the contact point reflects the weaker interaction between spheres. Since the interaction between spheres is proportional to the magnitude of the split, the higher m gives a smaller split. This is the reason why we observe a series of spiky peaks converging to the Mie resonance of a single sphere.

TABLE I. θ and ϕ dependence of normal field $\mathbf{F}_{l,m}^\beta$ in a single sphere. $f_m^\pm(\phi)$ is given by $f_m^\pm(\phi) = \exp(im\phi) \pm (-1)^{l\beta+I_{pol}} \exp(-im\phi)$. $I_{pol} = 1$ or 2 for the xz or the y polarization, and $I_\beta = 1$ or 2 for $\beta = N$ or M , respectively.

m	Mode	F_r	F_θ	F_ϕ
$m=0$	$N(\text{TM})$	P_l	$\partial P_l / \partial \theta$	–
	$M(\text{TE})$	–	–	$\partial P_l / \partial \theta$
$m>0$	$N(\text{TM})$	$f_m^+(\phi) P_l^m$	$f_m^+(\phi) \partial P_l^m / \partial \theta$	$f_m^-(\phi) m P_l^m / \sin \theta$
	$M(\text{TE})$	–	$f_m^-(\phi) m P_l^m / \sin \theta$	$f_m^+(\phi) \partial P_l^m / \partial \theta$

TABLE II. Number of maxima of $|P_l^m|$, $|mP_l^m/\sin \theta|$, and $|\partial P_l^m/\partial \theta|$ for $0 \leq \theta \leq \pi$.

Function	Maximum	$\theta=0, \pi$
$ P_l^m $	$l - m + 1$	0
$ mP_l^m/\sin \theta $	$l - m + 1$	0
$ \partial P_l^m/\partial \theta $	$l - m + 2$	0

^aMaximum for $m=0$.

^bHuge maximum for $m=1$. While it is 0 otherwise, peaks near $\theta=0$ or π are very large

^cVery sharp peak for $m=1$ only.

D. Bisphere apart

Finally, we study the dependence of the energy spectrum on the distance d between spheres. Figure 6(a) shows the energy spectra at $\theta=0^\circ$ for three cases of d : $d=0.1 \mu\text{m}$, $0.2 \mu\text{m}$, and $0.3 \mu\text{m}$. A drastic decrease of the split is observed with the increasing d . Simultaneously, the bonding and antibonding peaks become sharper. The decrease of the split is plotted in Fig. 6(b) as a function of d for 39TE1 and 39TM1 modes. The bonding and antibonding peaks are clearly distinguishable for small d . As d increases, both peaks merge into an exponentially decreasing straight line. This exponential decrease cannot be explained from the asymptotic behavior of the electric field outside the spheres. The field outside is described by the spherical Hankel function $h_l^{(1)}(k_0 r)$. If we take the distance between the center of each sphere as the characteristic length $r=2a_1$, we have $k_0 r=2k_0 a_1=2S \approx 56 \gg l=39$. Therefore, $h_l^{(1)}$ behaves as $(-i)^{l+1} \exp(ik_0 r)/k_0 r$, i.e., we found no evidence of the exponential dependence on d . This point is deeply related to the physical meaning of the overlap integral and will be clarified in the next section.

IV. SINGLE-MODE TIGHT-BINDING METHOD

Information on the MDR's of a bisphere in the previous section is utilized to establish the tight-binding description of the MDR in the following sections. As a first step, we present in this section its simplest form, i.e., single-mode tight-binding (SMTB) model. Though simple, it gives almost all the qualitative explanations of the characteristic features of MDR's in bisphere.

In analogy to the treatment of resonance d levels in the Korranga-Kohn-Rostoker (KKR) band theory of transition metals,³⁶ we extract a part of Eq. (2.3) relevant to the mode of concern, (β, l, m, n) . This gives the following set of equations for $\tilde{a}_{l,m}^{1,\beta}$ and $\tilde{a}_{l,m}^{2,\beta}$:

$$\begin{pmatrix} a_1^2 (\cot \delta_l^{1,\beta} - i) & -i a_2^2 A_{l,m;l,m}^{\beta,\beta}(k_0, \mathbf{R}^{21}) \\ -i a_1^2 A_{l,m;l,m}^{\beta,\beta}(k_0, \mathbf{R}^{12}) & a_2^2 (\cot \delta_l^{2,\beta} - i) \end{pmatrix} \begin{pmatrix} \tilde{a}_{l,m}^{1,\beta} \\ \tilde{a}_{l,m}^{2,\beta} \end{pmatrix} = \begin{pmatrix} \tilde{c}_{l,m}^{1,\beta} \\ \tilde{c}_{l,m}^{2,\beta} \end{pmatrix}. \quad (4.1)$$

This approximation is called the SMTB model. Before dealing with Eq. (4.1), we comment on the evaluation of $A_{l,m;l,m}^{\beta,\beta}$. In the preceding section, we have used the Mackowski recurrence relations¹³ to calculate $A_{l,m;p,m}^{\beta,\gamma}$ because we

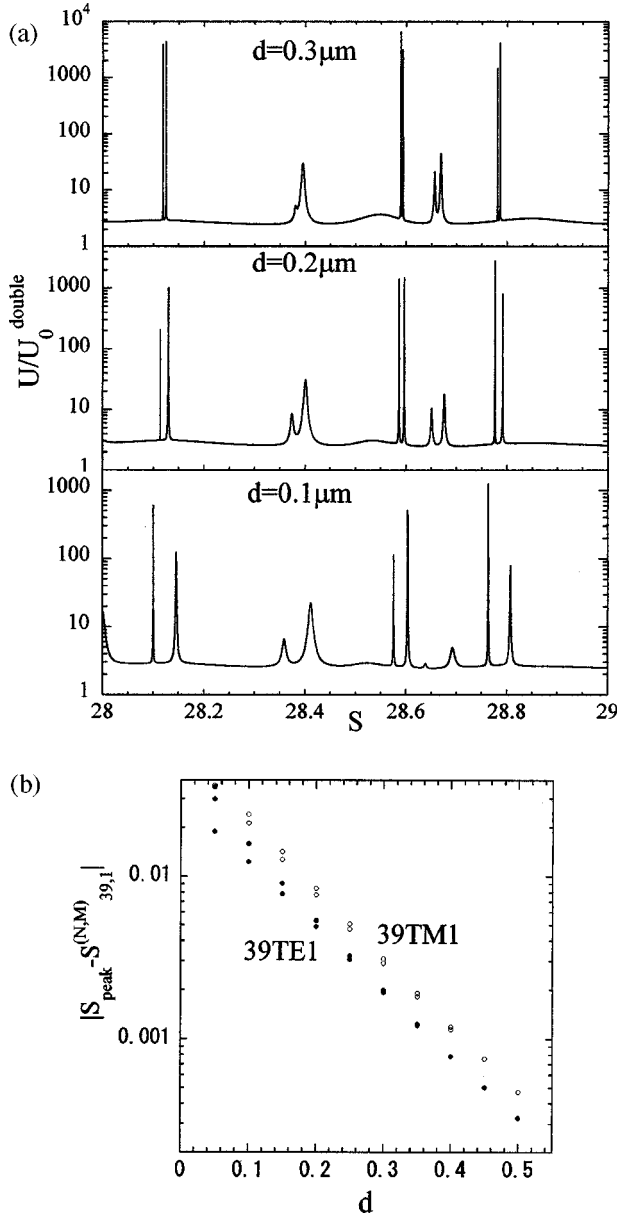


FIG. 6. (a) Internal energy spectra at $\theta=0^\circ$ for three cases of distance d between the spheres: $d=0.1 \mu\text{m}$, $d=0.2 \mu\text{m}$, and $d=0.3 \mu\text{m}$. (b) Shift of peak position S_{peak} at $\theta=0^\circ$ from the Mie resonance position $S_{l,n}^\beta$ as a function of the distance d for 39TE1 and 39TM1 modes. Note the logarithmic vertical scale in (b).

need the whole sets of $A_{l,m;p,m}^{\beta,\gamma}$. In the tight-binding formalism, in contrast, we need to evaluate $A_{l,m;p,m}^{\beta,\gamma}$ only for a few sets of (β, γ, l, p, m) . This can, in principle, be done by using the explicit expression of $A_{l,m;p,m}^{\beta,\gamma}$ in terms of the Wigner 3- j symbols³⁷ as given in Appendix C. However, the evaluation of the Wigners 3- j symbol needs careful numerical treatment because it is expressed as a sum of many terms containing factorials of large numbers. In this respect, it is much convenient and reliable to use the recurrence relation discovered by Bruning and Lo.⁹ Details are summarized in Appendix C. We also derive in Appendix C a simple estimation formula of $A_{l,m;p,m}^{\beta,\gamma}$ for $l, p \gg 1$ based on the maximum term approximation.

The solution to Eq. (4.1) is given as

$$\tilde{a}_{l,m}^{1,\beta} = \frac{1}{a_1^2} \frac{(\cot \delta_l^{2,\beta} - i) \tilde{c}_{l,m}^{1,\beta} + i A_{l,m;l,m}^{\beta,\beta}(k_0, \mathbf{R}^{21}) \tilde{c}_{l,m}^{2,\beta}}{\{(\cot \delta_l^{1,\beta} - i)(\cot \delta_l^{2,\beta} - i) + [A_{l,m;l,m}^{\beta,\beta}(k_0, \mathbf{R}^{21})]^2\}}, \quad (4.2a)$$

$$\tilde{a}_{l,m}^{2,\beta} = \frac{1}{a_2^2} \frac{(\cot \delta_l^{1,\beta} - i) \tilde{c}_{l,m}^{2,\beta} + i A_{l,m;l,m}^{\beta,\beta}(k_0, \mathbf{R}^{21}) \tilde{c}_{l,m}^{1,\beta}}{\{(\cot \delta_l^{1,\beta} - i)(\cot \delta_l^{2,\beta} - i) + [A_{l,m;l,m}^{\beta,\beta}(k_0, \mathbf{R}^{21})]^2\}}, \quad (4.2b)$$

where we have used the relation $A_{l,m;l,m}^{\beta,\beta}(k_0, \mathbf{R}^{12}) = A_{l,m;l,m}^{\beta,\beta}(k_0, \mathbf{R}^{21})$. This form of solution shows explicitly that the coefficient matrix of $\tilde{c}_{l,m}^{\beta}$ represents the response function whose pole gives the position of MDR in a bisphere within the SMTB model.³⁸ Note that the resonance positions are inherent in the system, i.e., they are independent of the excitation pattern:

$$(\cot \delta_l^{1,\beta} - i)(\cot \delta_l^{2,\beta} - i) + [A_{l,m;l,m}^{\beta,\beta}(k_0, \mathbf{R}^{21})]^2 = 0. \quad (4.3)$$

This is an implicit equation for the resonance wave number k_0 , but no solutions are found for real k_0 since $A_{l,m;l,m}^{\beta,\beta}(k_0, \mathbf{R}^{21})$ is generally complex. Therefore, we have to seek a real k_0 that gives a minimum for the left-hand side of Eq. (4.3). However, if we make the analytical continuation to the complex plane, the real and imaginary parts of the complex k_0 give the resonance wave number and the resonance width, respectively. We adopt this procedure below in an approximate way.

To simplify the analysis we focus on the identical spheres, i.e., $a_1 = a_2 = a$, $\varepsilon_1 = \varepsilon_2 = \varepsilon$, and $\delta_l^{1,\beta} = \delta_l^{2,\beta} = \delta_l^\beta$. Accordingly, Eqs. (4.2) are simplified as

$$\tilde{a}_{l,m}^{1,\beta} = \frac{1}{2a^2} \left\{ \frac{\tilde{c}_{l,m}^{1,\beta} + \tilde{c}_{l,m}^{2,\beta}}{\cot \delta_l^\beta - i - i A_{l,m;l,m}^{\beta,\beta}} + \frac{\tilde{c}_{l,m}^{1,\beta} - \tilde{c}_{l,m}^{2,\beta}}{\cot \delta_l^\beta - i + i A_{l,m;l,m}^{\beta,\beta}} \right\}, \quad (4.4a)$$

$$\tilde{a}_{l,m}^{2,\beta} = \frac{1}{2a^2} \left\{ \frac{\tilde{c}_{l,m}^{1,\beta} + \tilde{c}_{l,m}^{2,\beta}}{\cot \delta_l^\beta - i - i A_{l,m;l,m}^{\beta,\beta}} - \frac{\tilde{c}_{l,m}^{1,\beta} - \tilde{c}_{l,m}^{2,\beta}}{\cot \delta_l^\beta - i + i A_{l,m;l,m}^{\beta,\beta}} \right\}, \quad (4.4b)$$

where we use the abbreviation $A_{l,m;l,m}^{\beta,\beta} = A_{l,m;l,m}^{\beta,\beta}(k_0, \mathbf{R}^{21})$. Therefore, the MDR's of a bisphere within the SMTB model are given by the solutions of

$$\cot \delta_l^\beta = i(1 \pm A_{l,m;l,m}^{\beta,\beta}). \quad (4.5)$$

Since our aim is to give a simple expression of the MDR positions, we make further approximations. Firstly, from Appendix C, $A_{l,m;l,m}^{\beta,\beta}$ is approximately given for $l \gg 1$ and $l \gg k_0 |\mathbf{R}^{21}|$ by

$$A_{l,m;l,m}^{\beta,\beta} \cong i(-1)^{l+m} |A_{l,m;l,m}|, \quad (4.6)$$

where $A_{l,m;l,m}$ is defined in Appendix C. Second, we approximate $\cot \delta_l^\beta$ as follows: At the Mie resonance $S_{l,n}^\beta$, $\cot \delta_l^\beta = 0$ is satisfied. For higher-order resonances, $\cot \delta_l^\beta$ changes sign very rapidly within the narrow region around $S_{l,n}^\beta$. Therefore, we linearize $\cot \delta_l^\beta$ as

$$\cot \delta_l^\beta \cong - \frac{S - S_{l,n}^\beta}{\Delta_{l,n}^\beta}, \quad (4.7)$$

where $\Delta_{l,n}^\beta (>0)$ gives the Mie resonance width of mode (β, l, m, n) in a single sphere. They are obtained from Eqs. (2.4) and (2.5) as

$$\Delta_{l,n}^M = \frac{[kj_l(k_0a)j_l'(ka) - k_0j_l'(k_0a)j_l(ka)]^2}{(\varepsilon - 1)j_l^2(ka)}, \quad (4.8a)$$

$$\Delta_{l,n}^N = \frac{[k\psi_l(ka)\psi_l'(k_0a) - k_0\psi_l'(ka)\psi_l(k_0a)]^2}{(\varepsilon - 1)\{(\varepsilon k_0)^2[\psi_l'(ka)]^2 + l(l+1)[\psi_l(ka)]^2\}}, \quad (4.8b)$$

where $k_0 = S_{l,n}^\beta/a$ and $k = \sqrt{\varepsilon}k_0$. Substitution of Eqs. (4.6) and (4.7) into Eq. (4.5) yields an approximate formula of the MDR position within the SMTB model:

$$S \cong S_{l,n}^\beta - i\Delta_{l,n}^\beta \pm (-1)^{l+m}\Delta_{l,n}^\beta |A_{l,m;l,m}(S_{l,n}^\beta)|, \quad (4.9)$$

where $A_{l,m;l,m}(S_{l,n}^\beta) = A_{l,m;l,m}(k_0 = S_{l,n}^\beta/a, \mathbf{R}^{21})$. Note that the upper and lower signs correspond, respectively, to the denominator of the first and second terms in Eq. (4.4). This formula gives a qualitative guide to analyze a variety of phenomena observed in the MDR of the bisphere in Sec. III. The important point of this formula is that the overlap integral is explicitly given by $\Delta_{l,n}^\beta |A_{l,m;l,m}(S_{l,n}^\beta)|$.

Let us first estimate the magnitude of split between the bonding and antibonding modes within the SMTB model. From Eq. (4.9), the split is given by $2\Delta_{l,n}^\beta |A_{l,m;l,m}(S_{l,n}^\beta)|$. Numerical evaluation generally shows $\Delta_{l,n}^N > \Delta_{l,n}^M$, while $|A_{l,m;l,m}(S_{l,n}^N)| < |A_{l,m;l,m}(S_{l,n}^M)|$. For example, at $l=39$ and $m=1$ we have $\Delta_{l,1}^N = 1.4591 \times 10^{-6}$ and $\Delta_{l,1}^M = 0.9668 \times 10^{-6}$ while $A_{l,m;l,m} = 0.1037 + 27\,637.5997i$ ($29\,781.6326i$) for $\beta=N$ and $A_{l,m;l,m} = 0.0459 + 68\,128.4394i$ ($73\,167.6856i$) for $\beta=M$. Here, the values in the parentheses are given by the maximum term approximation in Appendix C. Thus, we have $2\Delta_{l,1}^M |A_{l,m;l,m}| = 0.1317$ (0.1415) and $2\Delta_{l,1}^N |A_{l,m;l,m}| = 0.0806$ (0.0869), in agreement with the observed values of 0.1284 for mode 39TE1 and 0.0927 for mode 39TM1.

The second problem is the m dependence of the split. We have concluded in Sec. III that the split is smaller for larger $|m|$. This conclusion is drawn from the behavior of the energy spectra and the contour maps of the internal field. Equation (4.9) now gives direct evidence for this, that is, $|A_{l,m;l,m}(S_{l,n}^\beta)|$ decreases with increasing $|m|$ as shown in Appendix C.

The third problem is the dependence of the split on the distance d between spheres. Since the split is given by $2\Delta_{l,n}^\beta |A_{l,m;l,m}(S_{l,n}^\beta)|$, it is enough to check the dependence of $|A_{l,m;l,m}|$ on d . In the maximum term approximation, $|A_{l,m;l,m}|$ is proportional to $h_{2l}^{(1)}[S_{l,n}^\beta(2+d/a)]$. For the present values of parameters, $(2l+1/2) > S_{l,n}^\beta(2+d/a)$ is satisfied so that $h_{2l}^{(1)}$ behaves as exponentially decreasing function. By using its asymptotic form, Eq. (C14), it is easy to show that

$$|A_{l,m;l,m}| \propto \exp\left\{-S_{l,n}^\beta \frac{d}{a} \left[\left(\frac{4l+1}{4S_{l,n}^\beta}\right)^2 - 1\right]^{1/2}\right\}. \quad (4.10)$$

This means that the split decreases exponentially with the increasing d in qualitative agreement with the results in Fig. 6(b).

The fourth problem deals with the internal field distribution of the bonding and antibonding states. The preceding section gave direct evidence that the lower and higher branches are the bonding and antibonding states, respectively. This is a natural consequence from the energetical consideration because a higher dielectric constant gives a stronger attractive potential for the electric field. However, this does not necessarily mean that all the bonding states are approximately given as $[\mathbf{F}_{l,m}^\beta(\mathbf{r}_1) + \mathbf{F}_{l,m}^\beta(\mathbf{r}_2)]/\sqrt{2}$. Here, $\mathbf{F}_{l,m}^\beta(\mathbf{r}_i)$ is the normal field of the sphere i given in Appendix D. Let us consider, for example, the case of $l+m = \text{even}$. Then, the term of lower sign in Eq. (4.9) gives the lower resonance. The lower sign corresponds to the second term in Eqs. (4.4). Neglecting the first term, we have $\tilde{a}_{l,m}^{1,\beta} \cong -\tilde{a}_{l,m}^{2,\beta}$. Thus, the bonding modes are given by $[\mathbf{F}_{l,m}^\beta(\mathbf{r}_1) - \mathbf{F}_{l,m}^\beta(\mathbf{r}_2)]/\sqrt{2}$. Now, the main component of the normal field in a single sphere has parity $(-1)^{l+m+1} = -1$ with $z \rightarrow -z$ except for three cases given in Appendix D. Therefore, when $l+m$ is even, the electric field of each sphere has the same sign at the contact point. This gives a large amplitude at the contact point in agreement with the intuitive interpretation of the bonding states. Note in this respect the observation in Fig. 5(d) that while the xz in-plane contour suggests an antibonding state, the contour within the yz plane looks like the bonding state. This corresponds to one of the three cases in Appendix D.

Finally, we discuss the peculiar excitation pattern of the energy spectrum at $\theta=90^\circ$ in Fig. 3(d). This is explained as follows: for 90° incidence, we have $\tilde{c}_{l,m}^{1,\beta} = \tilde{c}_{l,m}^{2,\beta}$. Therefore, the second term of Eq. (4.4) vanishes. This leads to $\tilde{a}_{l,m}^{1,\beta} = \tilde{a}_{l,m}^{2,\beta} \propto \tilde{c}_{l,m}^{1,\beta}$ ($= \tilde{c}_{l,m}^{2,\beta}$). It is easy to show that $\tilde{c}_{l,m}^\beta$ at $\theta=90^\circ$ vanishes when $l-m+I_{pol}+I_\beta$ is even. Here, $I_{pol}=1$ or 2 for xz polarization or y polarization and $I_\beta=1$ or 2 for $\beta=N$ or M , respectively. Therefore, $\tilde{a}_{l,m}^{1,\beta} = \tilde{a}_{l,m}^{2,\beta} = 0$ when $l-m+I_{pol}+I_\beta$ is even. For example, the case of the TM mode and xz polarization gives $I_{pol}+I_\beta=2$. Thus, $\tilde{a}_{l,m}^{1,\beta} = \tilde{a}_{l,m}^{2,\beta} = 0$ for even $l-m$. Now, the first term of Eq. (4.4) corresponds to the upper sign of Eq. (4.9). This gives the antibonding modes for even $l-m$. Therefore, the upper branch of the TM modes becomes silent for this type of excitation.

Thus, the SMTB model provides us with enough of a qualitative understanding of the MDR. However, a comparison with the exact numerical results of Sec. III reveals that the SMTB model is insufficient for the quantitative description of the MDR. Figure 7 shows the internal energy spectra of the exact calculation and the SMTB model at 10° incidence. We can see that the actual width of each peak is much broader than those of the SMTB model. In addition, a large shift of the bonding branch is observed for mode 39TM1. These problems drive us to improve the SMTB model, as will be described in the next section.

V. DOUBLE-MODE TIGHT-BINDING MODEL

The problem of the SMTB model can be easily overcome by extending the number of relevant modes (β, l, m, n) . This

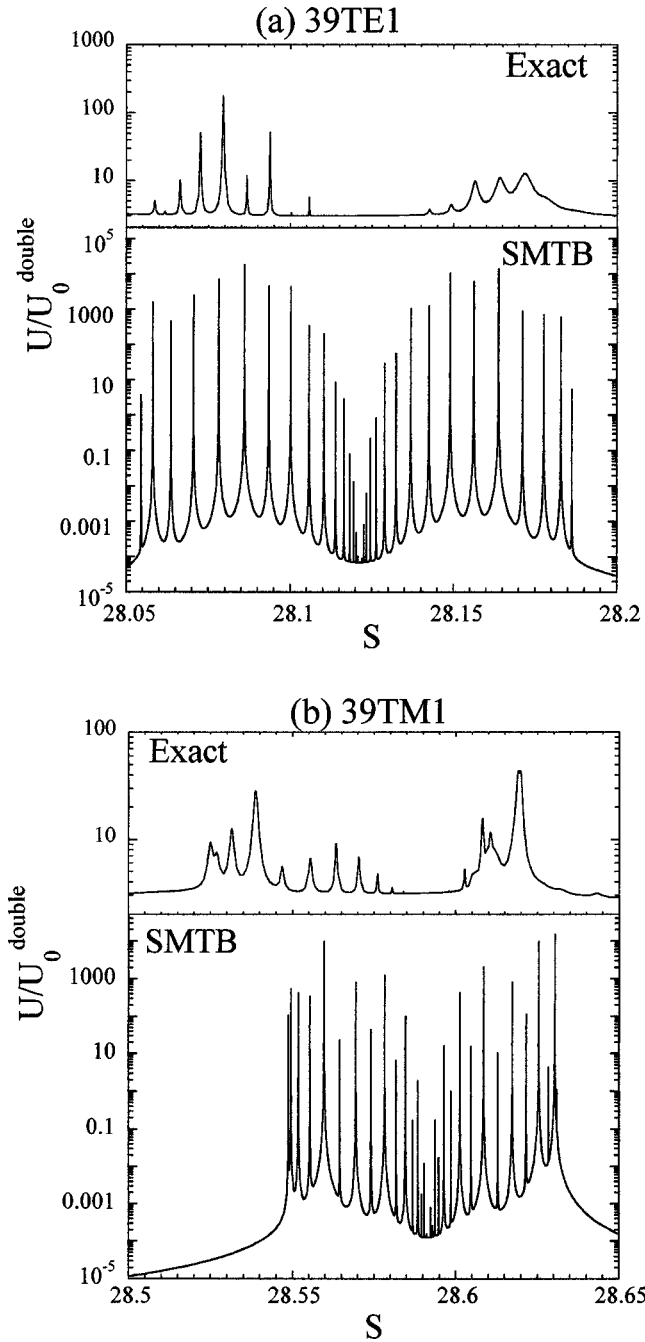


FIG. 7. Internal energy spectra of bisphere for (a) 39TE1 and (b) 39TM1 regions. Parameters are the same with those in Fig. 3(b) at $\theta=10^\circ$ with the xz polarization. The upper part of each figure represents the result of the exact calculation by taking $l_{max}=59$. The lower part is obtained by the SMTB model calculation.

is called the multimode tight-binding model. For example, a straightforward extension of Eq. (4.1) to include the modes in the range $19 \leq l \leq 54$ reproduces the results of the exact calculation fairly well with less computation time. However, when it is limited to $34 \leq l \leq 44$, the energy spectrum turns out to be spiky like that in Fig. 7. It would, therefore, be necessary to clarify the role of each mode, i.e., whether it would broaden or shift the relevant peak. With this knowledge we can reduce the number of the relevant modes as much as possible. In this section, we study the effect of each mode on resonances 39TE1 and 39TM1 by extending the

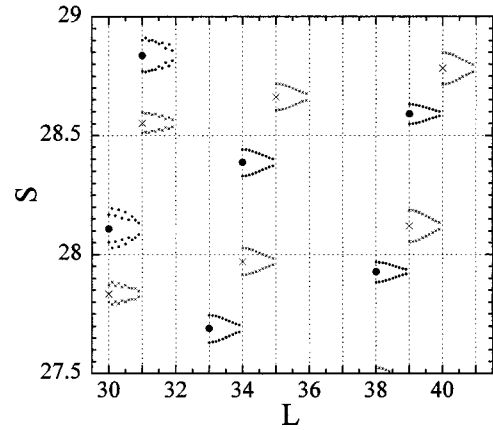


FIG. 8. Peak split of the Mie resonance in bisphere obtained by the SMTB model for $30 \leq l \leq 40$ in the range of $27.5 \leq S \leq 29$. Parameters are the same with those in Fig. 3(a). The large filled circles and crosses represent, respectively, the TM and TE Mie resonance positions of a single sphere. Each group of smaller symbols surrounding the large one shows the MDR peak positions of mode $0 \leq m \leq 9$. The mode $m=0$ (closest to the large symbol) has the largest split and the mode $m=9$ (furthest from the large symbol) has the smallest split.

SMTB model to the double-mode tight-binding (DMTB) model.

A. Preliminaries

Let us check the split of other modes in the bisphere within the SMTB model before going directly to the DMTB model. Figure 8 shows the bonding and antibonding branches for $30 \leq l \leq 40$ within the range $27.5 \leq S \leq 29$. Modes of up to $m=9$ are calculated. Large circles and crosses indicate the position of the Mie resonance of TM and TE modes, respectively. Small symbols surrounding large ones are the bonding and antibonding MDR modes of the bisphere. They are arranged in order from left to right as m increases from 0 to 9. Modes of $l=38,39,40$ are $n=1$ while those of $l=34,35$ and $l=30,31$ are $n=2$ and $n=3$, respectively.

As seen in the figure, the 34TE2 upper branch is very close in S to the 39TE1 lower branch. Therefore, their interaction is expected to be large. 30TM3 branches also overlap with 39TE1. Because of the higher value of n , however, the effect of mode 30TM3 on 39TE1 would not be significant. In addition, we will see in the next subsection that the interaction between modes of different β is much smaller than that of the same β . Therefore, mode 30TM3 is expected at most to broaden the peaks of mode 39TE1 because of its dissipative feature. This is also expected for the effect of mode 31TE3 on 39TM1. However, mode 35TE2 needs special attention. This mode is not so dissipative compared with the modes of $n=3$. In addition, its bonding branch overlaps with the antibonding branch of mode 39TM1. Therefore, these two branches are almost degenerate with each other. As in quantum mechanics, the degeneracy requires special treatment because even a small interaction gives a large split. Thus, mode 35TE2 is expected to have significant influence on mode 39TM1 although their interaction is small because of different β .

B. Double-mode tight-binding model

To understand the influence of other modes on resonances 39TE1 and 39TM1 we use the DMTB model. The DMTB

model is a straightforward extension of the SMTB model. We have simply to take account of two modes (β, l, m, n) and (β', l', m, n') in Eq. (2.3). For the bisphere composed of identical spheres, this procedure yields

$$\begin{pmatrix} \cot\delta_l^\beta - i & 0 & -iA_{l,m;l,m}^{\beta,\beta}(\mathbf{R}^{21}) & -iA_{l,m;l',m}^{\beta,\beta'}(\mathbf{R}^{21}) \\ 0 & \cot\delta_{l'}^{\beta'} - i & -iA_{l',m;l,m}^{\beta',\beta}(\mathbf{R}^{21}) & -iA_{l',m;l',m}^{\beta',\beta'}(\mathbf{R}^{21}) \\ -iA_{l,m;l,m}^{\beta,\beta}(\mathbf{R}^{12}) & -iA_{l,m;l',m}^{\beta,\beta'}(\mathbf{R}^{12}) & \cot\delta_l^\beta - i & 0 \\ -iA_{l',m;l,m}^{\beta',\beta}(\mathbf{R}^{12}) & -iA_{l',m;l',m}^{\beta',\beta'}(\mathbf{R}^{12}) & 0 & \cot\delta_{l'}^{\beta'} - i \end{pmatrix} \begin{pmatrix} \tilde{a}_{l,m}^{1,\beta} \\ \tilde{a}_{l',m}^{1,\beta'} \\ \tilde{a}_{l,m}^{2,\beta} \\ \tilde{a}_{l',m}^{2,\beta'} \end{pmatrix} = \begin{pmatrix} \tilde{c}_{l,m}^{1,\beta} \\ \tilde{c}_{l',m}^{1,\beta'} \\ \tilde{c}_{l,m}^{2,\beta} \\ \tilde{c}_{l',m}^{2,\beta'} \end{pmatrix}, \quad (5.1)$$

where we omit the common argument k_0 in the coefficient A 's.

While the analytical solution to Eq. (5.1) can be obtained, it is not so simple and transparent as in the case of the SMTB model. Instead, we use the energy spectrum at $\theta = 10^\circ$ with the xz polarization to pick out the peak positions of the bonding and antibonding modes of 39TE1 and 39TM1. In the calculation, we fix (β, l, m, n) at modes 39TE1 or 39TM1 and change other modes over the range of $30 \leq l' \leq 45$. The summation over m is taken in the range of $1 \leq m \leq 10$ for TE modes and $0 \leq m \leq 9$ for TM modes. Note the absence of mode $m=0$ for TE modes because $\tilde{c}_{l,m=0}^{i,\beta} = 0$ for odd values of $l_{pol} + l_\beta$. The peak positions in the energy spectrum are shown, respectively, in Figs. 9(a) and 9(b) for modes 39TE1 and 39TM1. In principle, the outermost peaks in the horizontal line of Figs. 9 correspond, respectively, to the $m=1$ mode of resonance 39TE1 and the $m=0$ mode of resonance 39TM1. However, we are unable to exclude tiny peaks due to other modes because of the use of energy spectra. These peaks appear irregularly, e.g., the leftmost point in the line of $l=30$ for the TM modes in Fig. 9(a).

As seen from the figures, modes of different β have almost no influence on the peak position of the relevant mode except for the cases of modes 35TE2 on 39TM1 and 34TE2 on 39TE1. This reflects the fact that $|A_{l,m;l',m}^{\beta,\beta'}|$ for $\beta \neq \beta'$ is much smaller than that for $\beta = \beta'$. Therefore, we concentrate on the cases of $\beta = \beta'$. Generally speaking, higher $|m|$ has less influence than lower $|m|$ since $|A_{l,m;l',m}^{\beta,\beta'}|$ decreases with increasing $|m|$. Peaks of mode 39TE1 are shifted to the higher side due to the interaction with modes $30 \leq l' \leq 34$. This is also the case for $36 \leq l' \leq 38$. The upshift is the largest for $l' = 34$. On the other hand, $l' = 35$ gives the downshift. Modes of $l' \geq 40$ generally give the downshift and their effect decreases with the increasing l' . This tendency also holds for the case of mode 39TM1 in Fig. 9(b).

We have also studied the peak broadening of modes 39TE1 and 39TM1 due to the interaction with other modes. It turns out that the modes of different β have negligible influence except for the case of mode 35TE2 on 39TM1. In the cases of the same β we found that the modes $l' \leq 35$ broaden both the bonding and antibonding modes while higher l' has a negligible influence on the peak width. Therefore, the broadening of the relevant mode occurs via the

interaction with the dissipative modes of lower order. In other words, they contribute mainly to the imaginary part of the poles of the response function.

Thus, the DMTB model enables us to classify each mode into two types. The first type is a mode that affects significantly both the peak position and the peak width of the relevant mode, resonance 35TE2 on 39TM1 or 34TE2 on 39TE1. These modes should be treated on equal footing with the relevant mode. The second type of mode gives only the peak shift or the peak broadening without changing the energy spectrum considerably. It is expected that the second type can be treated perturbationally as a reservoir mode, while the first one should be included as a relevant mode into the system.

In the perturbational treatment, the dynamics of the reservoir modes is irrelevant. In other words, we can neglect their S dependence and evaluate their contributions at a certain value of S , say, at the Mie resonance $S_{l,n}^\beta$ of the relevant mode. In fact, we found that this static treatment reproduces fairly well the peak shift and the peak broadening due to the modes of second type. The static treatment of the reservoir modes will be used in the next subsection to reduce the computation time significantly.

C. Improvement of DMTB: Perturbational inclusion of reservoir modes

To include the effect of the reservoir modes it is convenient to rewrite the basic equation (2.3) in the following matrix form:

$$P_{l,m}^\beta \tilde{\mathbf{a}}_{l,m}^\beta + \sum_{\beta'} \sum_{l' (\neq l)} Q_{l,m;l',m}^{\beta,\beta'} \tilde{\mathbf{a}}_{l',m}^{\beta'} = \tilde{\mathbf{c}}_{l,m}^\beta. \quad (5.2)$$

Here, we define the (2×2) matrices $P_{l,m}^\beta$ and $Q_{l,m;l',m}^{\beta,\beta'}$ as

$$P_{l,m}^\beta = \begin{pmatrix} a_1^2(\cot\delta_l^{1,\beta} - i) & -ia_1^2 A_{l,m;l,m}^{\beta,\beta}(k_0, \mathbf{R}^{21}) \\ -ia_2^2 A_{l,m;l,m}^{\beta,\beta}(k_0, \mathbf{R}^{12}) & a_2^2(\cot\delta_l^{2,\beta} - i), \end{pmatrix}, \quad (5.3a)$$

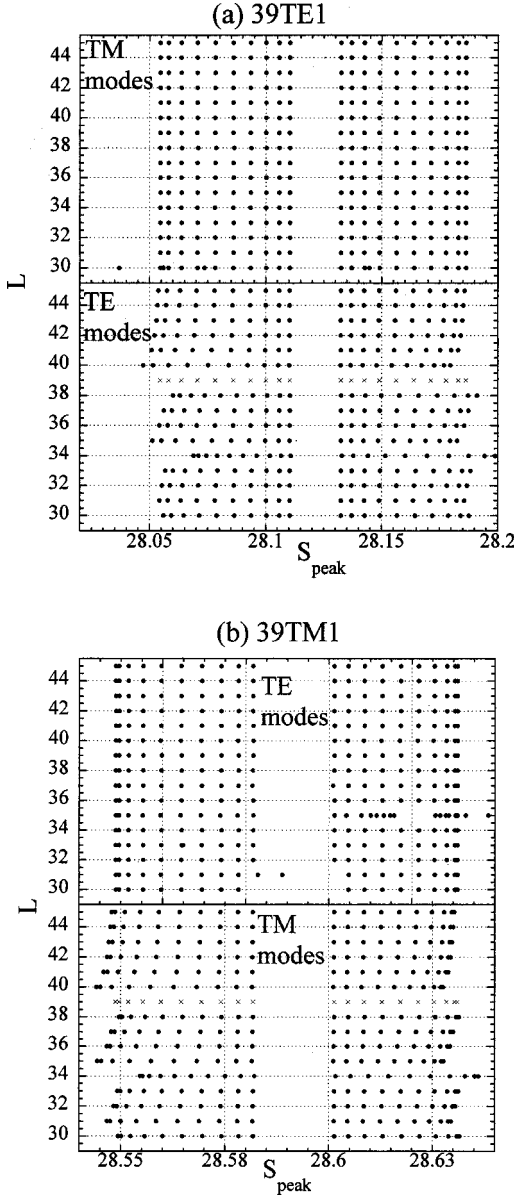


FIG. 9. Peak shift of (a) 39TE1 and (b) 39TM1 modes due to the interaction with other TE and TM modes. Peak positions are found from the internal energy spectra calculated by the DMTB model at $\theta = 10^\circ$ with the xz polarization. Parameters are the same with those in Fig. 3(b). The range of m is $1 \leq m \leq 10$ for the TE mode and $0 \leq m \leq 9$ for the TM mode. Outer peaks on the horizontal line correspond to the lower m . Crosses in the figures indicate the peak position of 39TE1 and 39TM1 modes obtained by the SMTB model.

$$Q_{l,m;l',m}^{\beta,\beta'} = \begin{pmatrix} 0 & -ia_1^2 A_{l,m;l',m}^{\beta,\beta'}(k_0, \mathbf{R}^{21}) \\ -ia_2^2 A_{l,m;l',m}^{\beta,\beta'}(k_0, \mathbf{R}^{12}) & 0 \end{pmatrix}. \quad (5.3b)$$

The vectors $\tilde{\mathbf{a}}_{l,m}^\beta$ and $\tilde{\mathbf{c}}_{l,m}^\beta$ in Eq. (5.2) are given as

$$\tilde{\mathbf{a}}_{l,m}^\beta = \begin{pmatrix} \tilde{a}_{l,m}^{1,\beta} \\ \tilde{a}_{l,m}^{2,\beta} \end{pmatrix}, \quad \tilde{\mathbf{c}}_{l,m}^\beta = \begin{pmatrix} \tilde{c}_{l,m}^{1,\beta} \\ \tilde{c}_{l,m}^{2,\beta} \end{pmatrix}. \quad (5.4)$$

Let us next introduce the (2×2) matrix $U_{l,m}^\beta$, which diagonalizes $P_{l,m}^\beta$:

$$U_{l,m}^\beta P_{l,m}^\beta (U_{l,m}^\beta)^{-1} = D_{l,m}^\beta. \quad (5.5)$$

By applying the transformation (5.5) to Eq. (5.2), we obtain

$$D_{l,m}^\beta \tilde{\alpha}_{l,m}^\beta + \sum_{\beta'} \sum_{l' (\neq l)} U_{l,m}^\beta Q_{l,m;l',m}^{\beta,\beta'} (U_{l',m}^{\beta'})^{-1} \tilde{\alpha}_{l',m}^{\beta'} = \tilde{\delta}_{l,m}^\beta, \quad (5.6)$$

where $\tilde{\alpha}_{l,m}^\beta$ and $\tilde{\delta}_{l,m}^\beta$ are given in terms of $\tilde{\mathbf{a}}_{l,m}^\beta$ and $\tilde{\mathbf{c}}_{l,m}^\beta$ as

$$\tilde{\alpha}_{l,m}^\beta = U_{l,m}^\beta \tilde{\mathbf{a}}_{l,m}^\beta, \quad \tilde{\delta}_{l,m}^\beta = U_{l,m}^\beta \tilde{\mathbf{c}}_{l,m}^\beta. \quad (5.7)$$

At this point, we divide the whole modes into the relevant mode (β, l) and the reservoir modes (γ, p) . Since the reservoir modes are treated perturbationally, the summation of the second term in Eq. (5.6) for the reservoir mode (γ, p) is restricted only over the relevant modes (β', l') . Therefore, $\tilde{\alpha}_{p,m}^\gamma$ is given in terms of $\tilde{\alpha}_{l',m}^{\beta'}$ as

$$\tilde{\alpha}_{p,m}^\gamma = (D_{p,m}^\gamma)^{-1} \tilde{\delta}_{p,m}^\gamma - (D_{p,m}^\gamma)^{-1} U_{p,m}^\gamma \times \sum_{\beta' \in \{\beta\}} \sum_{l' \in \{l\}} Q_{p,m;l',m}^{\gamma,\beta'} (U_{l',m}^{\beta'})^{-1} \tilde{\alpha}_{l',m}^{\beta'}. \quad (5.8)$$

Substitution of Eq. (5.8) into Eq. (5.6) for the relevant modes (β, l) yields a closed set of equations for $\{\tilde{\alpha}_{l,m}^\beta\}$:

$$\hat{D}_{l,m}^\beta \tilde{\alpha}_{l,m}^\beta + \sum_{\beta' \in \{\beta\}} \sum_{l' (\neq l)} U_{l,m}^\beta \hat{Q}_{l,m;l',m}^{\beta,\beta'} (U_{l',m}^{\beta'})^{-1} \tilde{\alpha}_{l',m}^{\beta'} = \tilde{\delta}_{l,m}^\beta. \quad (5.9)$$

Here, we define $\hat{D}_{l,m}^\beta$, $\hat{Q}_{l,m;l',m}^{\beta,\beta'}$, and $\tilde{\delta}_{l,m}^\beta$ as

$$\hat{D}_{l,m}^\beta = D_{l,m}^\beta - \sum_{\gamma,p} U_{l,m}^\beta Q_{l,m;p,m}^{\beta,\gamma} (U_{p,m}^\gamma)^{-1} (D_{p,m}^\gamma)^{-1} \times U_{p,m}^\gamma Q_{p,m;l,m}^{\gamma,\beta} (U_{l,m}^\beta)^{-1}, \quad (5.10a)$$

$$\hat{Q}_{l,m;l',m}^{\beta,\beta'} = Q_{l,m;l',m}^{\beta,\beta'} - \sum_{\gamma,p} Q_{l,m;p,m}^{\beta,\gamma} (U_{p,m}^\gamma)^{-1} (D_{p,m}^\gamma)^{-1} \times U_{p,m}^\gamma Q_{p,m;l',m}^{\gamma,\beta'}, \quad (5.10b)$$

$$\tilde{\delta}_{l,m}^\beta = \tilde{\delta}_{l,m}^\beta - \sum_{\gamma,p} U_{l,m}^\beta Q_{l,m;p,m}^{\beta,\gamma} (U_{p,m}^\gamma)^{-1} (D_{p,m}^\gamma)^{-1} \tilde{\delta}_{p,m}^\gamma. \quad (5.10c)$$

$\tilde{\alpha}_{p,m}^\gamma$ for the reservoir mode is obtained by substituting the solution of Eq. (5.9) into Eq. (5.8). This model is called the perturbed DMTB model.

The perturbational treatment of the reservoir modes significantly reduces the size of equation. In fact, we need only two relevant modes to reproduce the characteristic features of the energy spectra for resonances 39TE1 and 39TM1 as will be shown in the next subsection. We can also adopt the static treatment of the reservoir modes when the range of S is narrow. In this treatment, P 's and Q 's of Eqs. (5.3) having at least one reservoir index are evaluated at the Mie resonance of one of the relevant modes. The static treatment of reser-

voir modes further reduces the computation time by two orders of magnitude. Of course, the static treatment is not suitable for a wide range of S .

D. Numerical results

In this subsection, we give the numerical results of various quantities obtained by the perturbed DMTB model. The reservoir modes are chosen to cover $24 \leq p \leq 54$ and $\gamma = M, N$. The static treatment of the reservoir modes necessarily limits the range of S . Hence, we treat modes 39TE1 and 39TM1 separately. The Mie resonance position of modes 39TE1 and 39TM1 are, respectively, given by $S = 28.12142$ and $S = 28.59165$. An additional relevant mode is 34TE2 for 39TE1 and 35TE2 for 39TM1. It is, of course, possible to include more relevant modes. In this paper, however, we try to clarify the validity of the perturbed DMTB model and its limitation as well.

The energy spectrum obtained by the perturbed DMTB model is compared with that of the exact calculation in Fig. 10 at $\theta = 0^\circ$ and 10° with the xz polarization. In the perturbed DMTB model, the summation over m is taken for $0 \leq m \leq 20$ at $\theta = 10^\circ$. Compared with the SMTB model, significant improvement is observed for both the peak shift and the peak broadening. In particular, the perturbed DMTB model reproduces fairly well the asymmetric broadening of the bonding and antibonding modes of resonance 39TE1 at $\theta = 10^\circ$. It also gives the peculiar line shape of the antibonding branch of 39TM1 at $\theta = 10^\circ$. Note the difference of a small peak below $S = 28.05$ at $\theta = 0^\circ$ in Fig. 10(a). This peak is associated with the antibonding mode of resonance 34TE2. While 34TE2 is treated as the relevant mode, our main concern is mode 39TE1. In other words, other modes that interact strongly with mode 34TE2 are treated as the reservoir modes. This is the reason why this small peak is not well reproduced. The same is true for mode 35TE2, which appears as a shoulder below the antibonding peak of mode 39TM1 at $\theta = 0^\circ$.

In contrast to the internal energy spectrum, the total scattering cross section C_{total} does not agree well with the exact results as shown in Fig. 11 for the 39TE1 region. While the positions of sharp peaks and dips coincide with those of the exact results, its magnitude is greatly reduced. This is because we take no account of the modes $p \leq 23$ that would have a large contribution to C_{total} .

In Figs. 12 we compare the peak distribution of 39TE1 and 39TM1 modes obtained by the perturbed DMTB model and by the exact calculation. The incidence angle is chosen at $\theta = 0^\circ, 10^\circ, 45^\circ, 80^\circ$, and 90° . Some of the peaks obtained by the perturbed DMTB model are missing from the exact results. These peaks disappear because of either too much broadening or too low a peak intensity. Except for these peaks, the agreement with the exact results is satisfactory.

The perturbed DMTB model can also be used to analyze the dependence of the peak positions on the distance d between spheres. Figure 13 plots the peak positions in the 39TE1 and 39TM1 regions for $\theta = 0^\circ$ incidence. The perturbed DMTB model gives an exponential dependence of the peak positions on the distance d in excellent agreement with the exact results.

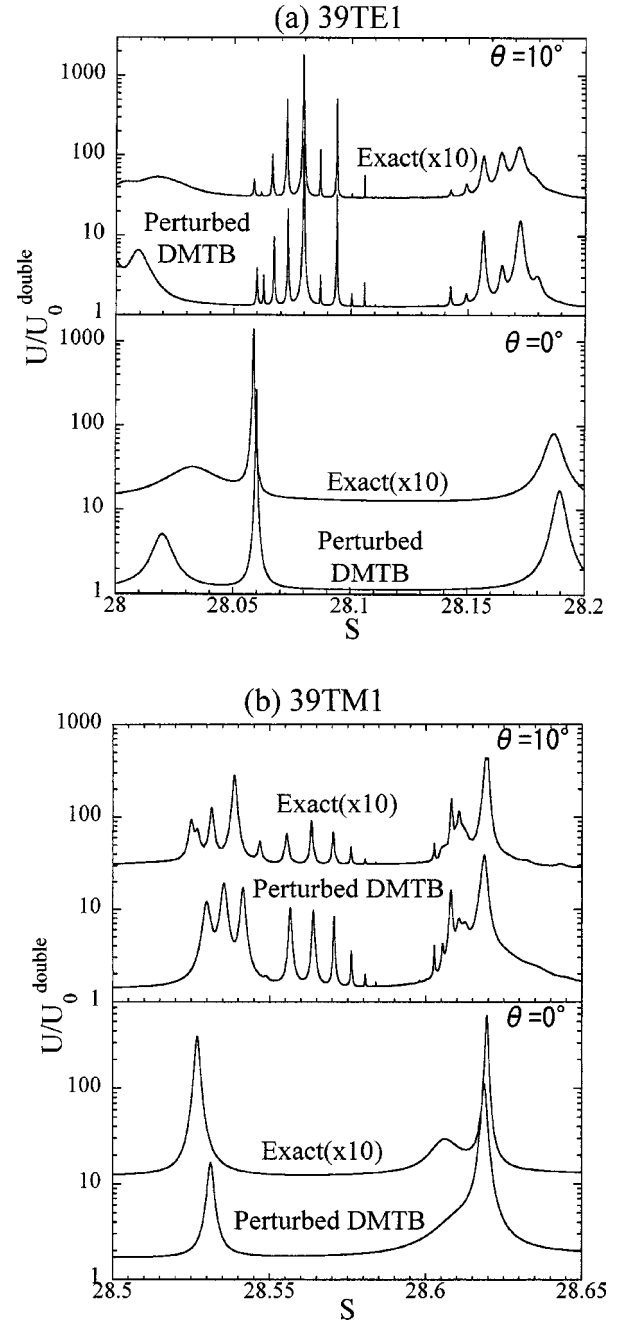


FIG. 10. Internal energy spectra of the (a) 39TE1 region and (b) 39TM1 region obtained by the exact calculation and by the perturbed DMTB model. Parameters are the same with those in Fig. 3. The energy spectra of the exact results are multiplied by 10 as a guide for the eye.

It would be interesting to study the level-crossing phenomenon induced by the change of the second radius a_2 . The two spheres are in contact and a_1 is kept at $2.5 \mu\text{m}$. The results are plotted in Fig. 14 at $\theta = 0^\circ$. The filled circles and the crosses show the peak positions at each radius a_2 by the exact calculation and by the perturbed DMTB model, respectively. The vertical axis is $S = k_0 a_1$. Note that the smaller value of a_2 pushes up the resonance wave number of the second sphere $k_0 = S_{l,n}^\beta / a_2$ so that the Mie resonance of the second sphere appears at higher $S = k_0 a_1 = S_{l,n}^\beta a_1 / a_2$. The level crossing of the 39TE1 and 39TM1 modes shows a

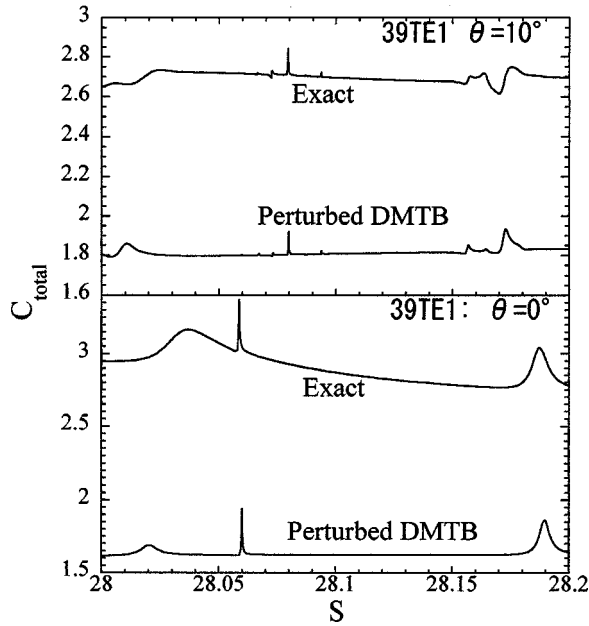


FIG. 11. Comparison of the normalized total scattering cross sections C_{total} in the 39TE1 region between the exact results and those obtained by the perturbed DMTB model. Parameters are the same with those in Fig. 10.

rather complicated behavior owing to the presence of modes 34TE2 and 35TE2. This complicated level-crossing phenomenon involving modes 34TE2 and 35TE2 is reproduced by the perturbed DMTB model when a_2 is close to a_1 . However, some of the peaks are missing in the perturbed DMTB model. If one wants to achieve better agreement, one would simply extend the DMTB model to the multimode tight-binding model. For example, the multimode tight-binding calculation including 12 relevant modes, $l = 31, 34, 35, 38, 39, 40$ and $\beta = N, M$ is enough to reproduce almost all the features of the level crossing shown in Fig. 14.

Finally, we compare the internal field distribution. We pick out some of the peaks in the energy spectra obtained by the perturbed DMTB model. Their mode number m_0 can be identified by a direct comparison of $a_{l,m}^{i,\beta}$. Then, we evaluate the electric field by the perturbed DMTB model, using a pair of m_0 and $-m_0$. It turns out that the single use of m_0 fails to give the characteristic feature of the exact contour maps except for the case of $\theta = 0^\circ$ incidence. This is due to the interference of the electric fields between different m components. Therefore, we sum up the field contribution over an appropriate range of m including m_0 . Figures 15(a) and 15(b), respectively, show the contour maps of the internal field at the bonding and antibonding peaks of mode 39TE1 for $\theta = 0^\circ$ incidence. Figure 15(c) corresponds to the case of Fig. 5(f) (39TE1, $\theta = 45^\circ$, $m_0 = 18$). Here, we take the sum over m in the range $13 \leq m \leq 23$. A comparison with the exact results reveals that the essential features of the contour maps are reproduced well such as the bonding and antibonding states of the electric field at the contact point. It is commonly observed that the central part of each sphere has lower electric field than that of the exact result. This is simply because we take no account of the lower resonance modes, i.e., $l \leq 23$ are neglected. These modes have a larger electric field in the inner part of the spheres.

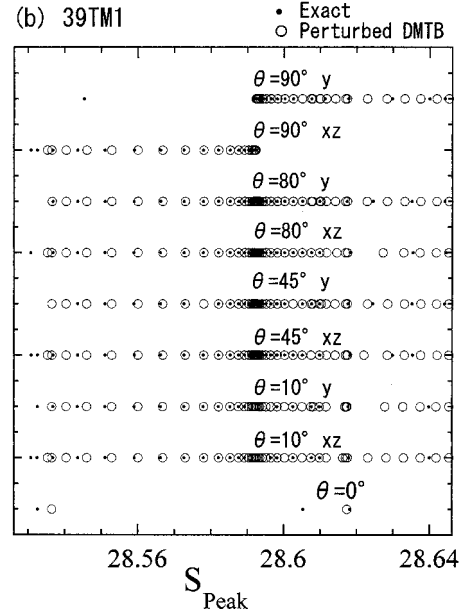
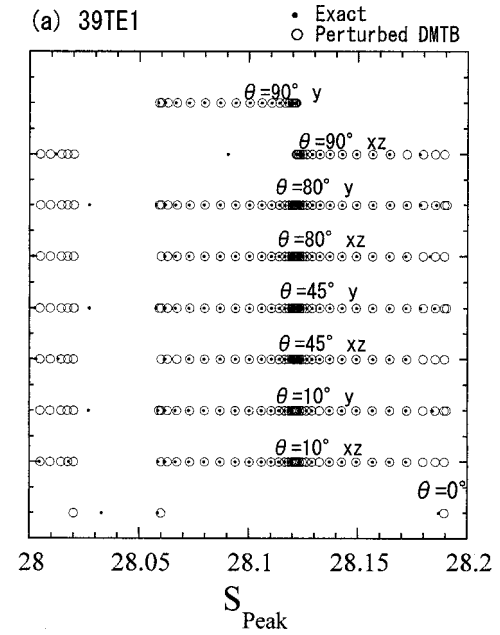


FIG. 12. Peak positions of the exact results and those obtained by the perturbed DMTB model for various incidence angles and polarizations in the (a) 39TE1 region and (b) 39TM1 region in (b). Exact results and those by the perturbed DMTB model are, respectively, denoted by the small filled circles and the empty large circles. They are grouped and put on the same horizontal line according to the incidence angle and the polarization indicated just above each line. Parameters of the spheres are the same with those in Fig. 3.

VI. DISCUSSION AND SUMMARY

While the DMTB model fails to give the correct peak positions, it provides us with a powerful tool to analyze the peculiar line shape of the antibonding state of mode 39TM1 at $\theta = 10^\circ$. In addition, it gives a qualitative explanation of the peak shift of modes 39TE1 and 39TM1 due to the interaction with other modes. Let us first consider the former case. We choose modes 39TM1 and 35TE2 and calculate the energy spectrum at $\theta = 10^\circ$ with the xz polarization by the

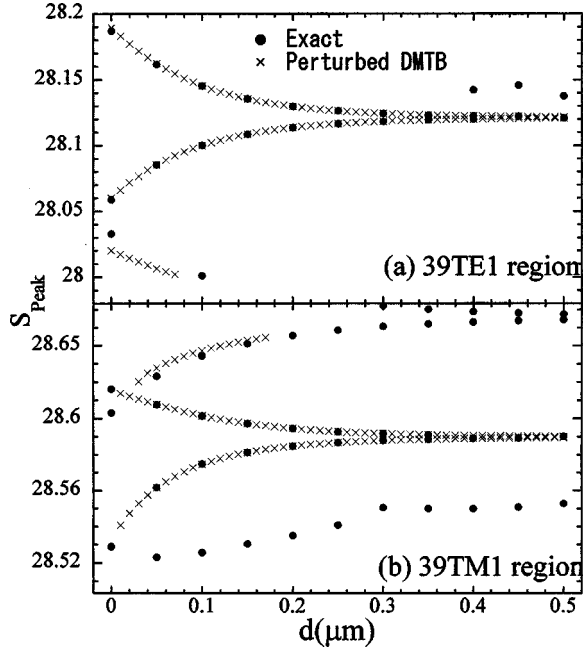


FIG. 13. Peak positions vs distance d between spheres for (a) 39TE1 and (b) 39TM1 modes at $\theta=0^\circ$. Filled circles and crosses represent, respectively, the exact results and those by the perturbed DMTB model. Parameters are the same as those in Fig. 6.

DMTB model. The summation over m is taken for $0 \leq m \leq 10$. The results are shown in Fig. 16 by the thick line. The individual contribution from $2 \leq m \leq 7$ is also plotted by the thin line multiplied by an appropriate factor as a guide for the eye. As is seen, the bonding branch shows no peculiar

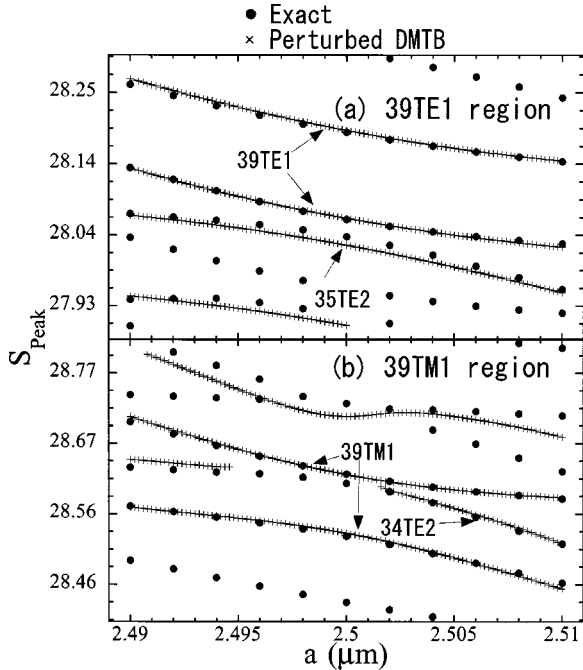


FIG. 14. Level crossing as a function of the radius of the second sphere a_2 at $\theta=0^\circ$ for the (a) 39TE1 region and (b) 39TM1 region. The spheres are in contact and the radius of the first sphere is fixed at $a_1=2.5 \mu\text{m}$. Both spheres have the same dielectric constant $\epsilon_1 = \epsilon_2 = (1.59)^2$. Filled circles represent the exact results and crosses show the results by the perturbed DMTB model.

behavior, i.e., it is very similar to that of the SMTB model in Fig. 7(b) though it is shifted to the lower side. The antibonding branch, on the other hand, consists of sharp and broad peaks. In particular, peaks around $S=28.62$ are missing. This behavior is due to the level crossing between the bonding modes of 35TE2 and the antibonding modes of 39TM1. Clear evidence of their coexistence is seen for $m=2$ in the region of $28.6 \leq S \leq 28.64$. The lower broad peak and the upper sharp peak correspond, respectively, to the $m=2$ modes of resonances 35TE2 and 39TM1. As m increases, the bonding peak of mode 35TE2 shifts to the higher side while that of 39TM1 moves downward. These peaks are almost degenerate at $m=4$ or 5. Due to the interaction, both peaks have almost the same width. This peak width is determined by the dissipation due to 35TE2 mode. The disappearance of peaks around $S=28.62$ is nothing but the repulsion between the almost-degenerate peaks. Thus, the origin of the peculiar behavior of the antibonding branch is attributed to the level crossing with the mode 35TE2.

To discuss the peak shift of (β, l, m, n) mode due to the interaction with (β', l', m, n') mode we decouple Eqs. (5.1) as follows:

$$\begin{pmatrix} \cot \delta_l^\beta - i - iA_{l,m;l,m}^{\beta,\beta} & -i\eta A_{l,m;l',m}^{\beta,\beta'} \\ -iA_{l',m;l,m}^{\beta',\beta} & \cot \delta_{l'}^{\beta'} - i - i\eta A_{l',m;l',m}^{\beta',\beta'} \end{pmatrix} \times \begin{pmatrix} \tilde{a}_{l,m}^{1,\beta} + \tilde{a}_{l,m}^{2,\beta} \\ \tilde{a}_{l',m}^{1,\beta'} + \eta \tilde{a}_{l',m}^{2,\beta'} \end{pmatrix} = \begin{pmatrix} \tilde{c}_{l,m}^{1,\beta} + \tilde{c}_{l,m}^{2,\beta} \\ \tilde{c}_{l',m}^{1,\beta'} + \eta \tilde{c}_{l',m}^{2,\beta'} \end{pmatrix}, \quad (6.1a)$$

$$\begin{pmatrix} \cot \delta_l^\beta - i + iA_{l,m;l,m}^{\beta,\beta} & i\eta A_{l,m;l',m}^{\beta,\beta'} \\ iA_{l',m;l,m}^{\beta',\beta} & \cot \delta_{l'}^{\beta'} - i + i\eta A_{l',m;l',m}^{\beta',\beta'} \end{pmatrix} \times \begin{pmatrix} \tilde{a}_{l,m}^{1,\beta} - \tilde{a}_{l,m}^{2,\beta} \\ \tilde{a}_{l',m}^{1,\beta'} - \eta \tilde{a}_{l',m}^{2,\beta'} \end{pmatrix} = \begin{pmatrix} \tilde{c}_{l,m}^{1,\beta} - \tilde{c}_{l,m}^{2,\beta} \\ \tilde{c}_{l',m}^{1,\beta'} - \eta \tilde{c}_{l',m}^{2,\beta'} \end{pmatrix}. \quad (6.1b)$$

Here, $\eta = (-1)^{l+l'+l_\beta+l_{\beta'}}$ and arguments in A 's are commonly given by (k_0, \mathbf{R}^{21}) . In the decoupling procedure, we use the symmetry property of A 's with respect to the inversion $\mathbf{R}^{12} \rightarrow \mathbf{R}^{21}$ in Appendix C. From the viewpoint of the response function, it is enough to study the complex zeros of the determinant of coefficient matrices in Eqs. (6.1). Let us focus on the case of $\beta' = \beta$. To simplify the analysis all the parameters except for $\cot \delta_l^\beta$ are evaluated at the Mie resonance $S_{l,n}^\beta$. This evaluation is denoted by the superscript 0. Then, the determinant of Eq. (6.1a) gives

$$\cot \delta_l^\beta = i + iA_{l,m;l,m}^0 - \frac{\eta A_{l,m;l',m}^0 A_{l',m;l,m}^0}{\cot(\delta_{l'}^{\beta'})^0 - i - i\eta A_{l',m;l',m}^0}. \quad (6.2)$$

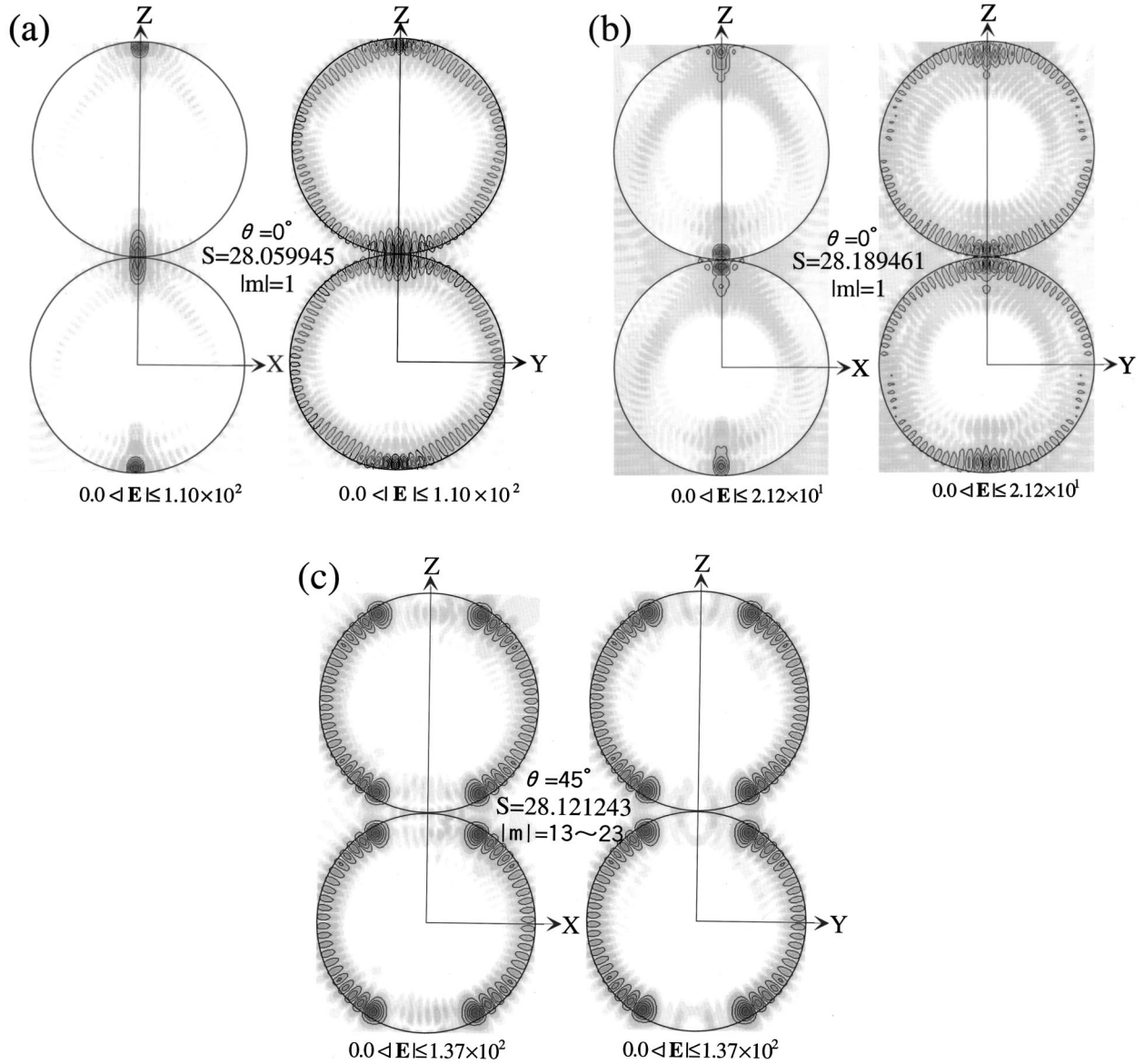


FIG. 15. Distribution of the electric field $|\mathbf{E}|$ within the xz and the yz planes ($-a \leq x, y \leq a$, $-a \leq z \leq 3a$) at some of the MDR peaks of the energy spectra by the perturbed DMTB model. The field distributions are also calculated by the perturbed DMTB model. The incident field is polarized within the xz plane. The darker region corresponds to the higher field. (a) and (b) are the bonding and antibonding states of the 39TE1 mode at $\theta = 0^\circ$. The peak for (c) is chosen from a dense collection of peaks centering at the Mie resonance of mode 39TE1 at $\theta = 45^\circ$. (a), (b), and (c) correspond respectively to (a), (b), and (f) in Fig. 5.

This equation is further simplified by the linearization of $\cot \delta_{l'}^\beta$, Eq. (4.7), and the following relation from Eqs. (C7) and (C16) of Appendix C:

$$\begin{aligned} A_{l',m;l,m} &= (-1)^{l+l'} \frac{l(l+1)}{l'(l'+1)} A_{l,m;l',m} \\ &\cong i(-1)^{l+m} \frac{l(l+1)}{l'(l'+1)} |A_{l,m;l',m}|. \end{aligned} \quad (6.3)$$

Here, the last approximation holds for $l, l' \gg 1$ and $l+l' > 2ak_0$. Thus, the MDR position of (β, l, m, n) mode within the DMTB model is given by

$$S = S_{l,n}^\beta - i\Delta_{l,n}^\beta + (-1)^{l+m} \Delta_{l,n}^\beta |A_{l,m;l,m}| + \Delta S_{l,n}^\beta, \quad (6.4a)$$

$$\Delta S_{l,n}^\beta \cong -\frac{l(l+1)}{l'(l'+1)} \Delta_{l,n}^\beta \frac{|A_{l,m;l',m}^0|^2}{\cot(\delta_{l'}^{\beta'})^0 - i + (-1)^{l+m} |A_{l',m;l',m}^0|}. \quad (6.4b)$$

Replacement of $(-1)^{l+m} \rightarrow -(-1)^{l+m}$ gives the solution to Eq. (6.1b).

Obviously, the peak shift hinges on the sign of the real and imaginary parts of $\Delta S_{l,n}^\beta$. The denominator of $\Delta S_{l,n}^\beta$ is generally governed by $\cot(\delta_{l'}^{\beta'})^0$. The Mie resonance positions of modes $l' \geq 40$ are much higher than those of positions 39TE1 and 39TM1. In this case, $\cot(\delta_{l'}^{\beta'})^0$ gives a large positive value and dominates the denominator of $\Delta S_{l,n}^\beta$. Thus, $\Delta S_{l,n}^\beta$ becomes negative and the peaks of modes 39TE1 and 39TM1 move downward. In addition, the peak

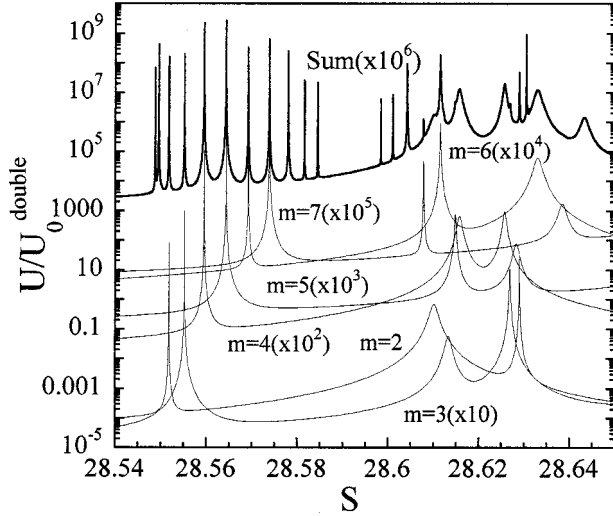


FIG. 16. Energy spectrum of 39TM1+35TE2 modes obtained by the DMTB model. The incidence angle is chosen at $\theta = 10^\circ$ with the xz in-plane polarization. Thick line shows the energy summed over $0 \leq m \leq 10$. The contribution from each m is plotted by thin line with an appropriate scale factor as a guide for the eyes.

shift decreases rapidly with the increasing l' because of the huge increase of $\cot(\delta_{l'}^{\beta'})^0$. Mode $l' = 38$, on the other hand, has a Mie resonance at $S = 27.45876$ and 27.92836 so that $\cot(\delta_{l'}^{\beta'})^0$ gives a large negative value. Therefore, $\Delta S_{l,n}^{\beta}$ becomes positive and pushes up the peak positions. This is also the case for $l' = 34$, which has a Mie resonance at $S = 27.97029$ and 28.38742 . In this approximation, therefore, the peak shift due to mode (β', l', m, n') is mainly determined by the denominator of $\Delta S_{l,n}^{\beta}$. The decrease of $\Delta S_{l,n}^{\beta}$ with the increase of $|m|$ is due to its numerator $|A_{l,m;l',m}^0|^2$.

Peak width is determined by $|\Delta_{l,n}^{\beta} + \text{Im}(\Delta S_{l,n}^{\beta})|$. Within the present approximation, $\text{Im}(\Delta S_{l,n}^{\beta})$ is always negative and broadens the peak. However, its magnitude is too small to account for the exact results. To analyze the peak broadening, therefore, we have to use at least the perturbed DMTB model.

In summary, we have studied the MDR's of a bisphere in detail from the viewpoint of the electromagnetic energy stored in the bisphere. Compared with the scattering cross sections, we observe a series of clear resonances in the internal energy spectrum. The energy spectrum is composed of the bonding and antibonding branches originating from the Mie resonance of each sphere. These branches are composed of sharp peaks owing to the removal of the degeneracy with respect to m . For higher m , the split between the bonding and antibonding modes becomes smaller. The bonding and antibonding states are visualized in a series of contour maps of the internal electric field. The analysis of the energy spectrum is based on the *ab initio* tight-binding formalism. The present formalism provides us with a simple interpretation of the overlap integral in the photonic version. The SMTB model gives a qualitative explanation of various characteristics of the energy spectra. We also present the perturbed DMTB model, which incorporates the dissipative nature of the lower-order resonance modes. Almost all the characteristic features are reproduced by the perturbed DMTB model.

The application of the present formalism to a cluster of spheres such as triangular or tetrahedral configurations is straightforward. Also we can apply the present formalism to the photonic band-structure calculation of the higher-order resonance in 1D, 2D, and 3D systems. These applications are now in progress.

ACKNOWLEDGMENTS

The authors acknowledge S. Kuwata-Gonokami and T. Mukaiyama for detailed experimental aspects of the MDR's in bisphere. They are also grateful for fruitful and impressive discussions with K. Ohtaka. One of the authors (H. M.) expresses sincere gratitude to E. C. for his continuous encouragement and profound inspiration. This work was supported by the Grant-in-Aid for Scientific Research from the Ministry of Education, Science and Culture.

APPENDIX A: VECTOR SPHERICAL HARMONICS

The vector spherical harmonics (VSH's) $\mathbf{E}_{l,m}^{\beta}(f_l, kr, \theta, \phi)$ are solutions of the Maxwell equation suitable for the spherical boundary condition.^{3,35} They are defined by

$$\mathbf{E}_{l,m}^M(f_l, kr, \theta, \phi) = f_l(kr) \left(\mathbf{e}_\theta \frac{im}{\sin \theta} - \mathbf{e}_\phi \frac{\partial}{\partial \theta} \right) Y_{l,m}(\theta, \phi), \quad (\text{A1a})$$

$$\begin{aligned} \mathbf{E}_{l,m}^N(f_l, kr, \theta, \phi) &= \mathbf{e}_r \frac{f_l(kr)}{kr} l(l+1) Y_{l,m}(\theta, \phi) \\ &+ \frac{1}{kr} \frac{d}{d(kr)} [kr f_l(kr)] \\ &\times \left(\mathbf{e}_\theta \frac{\partial}{\partial \theta} + \mathbf{e}_\phi \frac{im}{\sin \theta} \right) Y_{l,m}(\theta, \phi), \end{aligned} \quad (\text{A1b})$$

where $f_l(kr)$ is either the spherical Bessel function $j_l(kr)$ or the spherical Hankel function of the first kind $h_l^{(1)}(kr)$. $\mathbf{E}_{l,m}^M$ and $\mathbf{E}_{l,m}^N$ are, respectively, called the transverse electric (TE) mode and the transverse magnetic (TM) mode. These VSH's form a complete set of the Maxwell equations in a uniform dielectric medium. $\mathbf{E}_{l,m}^{\beta}$ satisfies the following orthogonal relation with respect to θ and ϕ :

$$\begin{aligned} &\int d\Omega [\mathbf{E}_{l,m}^{\beta}(f_l, kr, \theta, \phi)]^* \mathbf{E}_{p,q}^{\gamma}(f_p, kr, \theta, \phi) \\ &= \delta_{l,p} \delta_{m,q} \delta_{\beta,\gamma} \frac{l(l+1)}{(2l+1)} \\ &\times \begin{cases} (2l+1) |f_l(kr)|^2 & \text{for } \beta=M, \\ |f_{l+1}(kr)|^2 + (l+1) |f_{l-1}(kr)|^2 & \text{for } \beta=N. \end{cases} \end{aligned} \quad (\text{A2})$$

In the definition of the VSH's, we use the spherical harmonic $Y_{l,m}$. $Y_{l,m}$ is defined with the associated Legendre function P_l^m . There are two types of definition for P_l^m , i.e., Hobson's definition and Ferrers's definition.³⁹ In the present

paper, we adopt Ferrers's definition. To avoid confusion we give below their explicit form:

$$Y_{l,m}(\theta, \phi) \equiv (-1)^m \sqrt{\frac{2l+1}{4\pi} \frac{(l-m)!}{(l+m)!}} P_l^m(\cos\theta) \times \exp(im\phi) \quad (-m \leq l \leq m), \quad (\text{A3})$$

where P_l^m is given for $m \geq 0$ as

$$P_l^m(x) \equiv \frac{(1-x^2)^{m/2}}{2^l l!} \frac{d^{l+m}}{dx^{l+m}} (x^2-1)^l. \quad (\text{A4})$$

P_l^m for $m < 0$ is defined via P_l^{-m} by

$$P_l^m(x) \equiv (-1)^m \frac{(l+m)!}{(l-m)!} P_l^{-m}(x). \quad (\text{A5})$$

APPENDIX B: VSH EXPANSION OF PLANE ELECTROMAGNETIC WAVE

The explicit form of the expansion coefficient $c_{l,m}^\beta$ for the plane-wave electromagnetic field in Eq. (2.1c) was derived by several authors.^{8,40} We give below their explicit expression in terms of the spherical harmonics.

$$\begin{aligned} c_{l,m}^N = \frac{4\pi i^{l-1}}{l(l+1)} & \left\{ \left[-l \sqrt{\frac{(l-m+2)(l-m+1)}{(2l+3)(2l+1)}} Y_{l+1,m-1}^*(\hat{\mathbf{k}}) \right. \right. \\ & \left. \left. - (l+1) \sqrt{\frac{(l+m)(l+m-1)}{(2l+1)(2l-1)}} Y_{l-1,m-1}^*(\hat{\mathbf{k}}) \right] E_0^- \right. \\ & \left. + \left[l \sqrt{\frac{(l+m+2)(l+m+1)}{(2l+3)(2l+1)}} Y_{l+1,m+1}^*(\hat{\mathbf{k}}) \right. \right. \\ & \left. \left. + (l+1) \sqrt{\frac{(l-m)(l-m-1)}{(2l+1)(2l-1)}} Y_{l-1,m+1}^*(\hat{\mathbf{k}}) \right] E_0^+ \right. \\ & \left. + \left[-l \sqrt{\frac{(l+m+1)(l-m+1)}{(2l+3)(2l+1)}} Y_{l+1,m}^*(\hat{\mathbf{k}}) \right. \right. \\ & \left. \left. + (l+1) \sqrt{\frac{(l+m)(l-m)}{(2l+1)(2l-1)}} Y_{l-1,m}^*(\hat{\mathbf{k}}) \right] E_0^z \right\}. \quad (\text{B1}) \end{aligned}$$

Here, $\hat{\mathbf{k}} = \mathbf{k}/|\mathbf{k}|$ and $E_0^\pm = \frac{1}{2}(E_0^x \pm iE_0^y)$. $c_{l,m}^M$ can be immediately obtained from the above formula by changing $E_0^\pm \rightarrow H_0^\pm = \frac{1}{2}(H_0^x \pm iH_0^y)$, $E_0^z \rightarrow H_0^z$ and multiplying i on the right-hand side.

A simple relation exists between $c_{l,m}^\beta$ and $c_{l,-m}^\beta$. Suppose that \mathbf{k} lies on the xz plane and all the components of \mathbf{E}_0 are real. Then, it is easy to show by using Eq. (B1) that

$$c_{l,m}^\beta = (-1)^{l+I_{pol}} (c_{l,m}^\beta)^*, \quad c_{l,-m}^\beta = (-1)^{l+m+I_\beta} (c_{l,m}^\beta)^*, \quad (\text{B2})$$

where I_{pol} is either 1 or 2 corresponding to the xz or y polarization, and I_β is 1 or 2 for $\beta=N$ or $\beta=M$, respectively. From these two relations we have

$$c_{l,-m}^\beta = (-1)^{m+I_\beta+I_{pol}} c_{l,m}^\beta. \quad (\text{B3})$$

By applying the relations (B3) for $c_{l,m}^\beta$ and (C7c) for $A_{l,m;p,m}^{\gamma,\beta}(k_0, \mathbf{R}^{ij})$ to Eq. (2.3), we have

$$a_{l,-m}^{i,\beta} = (-1)^{m+I_\beta+I_{pol}} a_{l,m}^{i,\beta}. \quad (\text{B4})$$

This shows the degeneracy of the internal energy with respect to m and $-m$ because it depends only on $|a_{l,m}^{i,\beta}|^2$. The relation (B3) will also be used in Appendix D to classify the normal states of Mie resonance in a single sphere.

APPENDIX C: VECTOR ADDITION THEOREM

The vector addition theorem has been treated in a variety of work.²⁴⁻²⁶ In this paper we use the coefficient $A_{l,m;p,m}^{\gamma,\beta}$ in two ways. One is for the exact numerical calculation and the other is for the tight-binding calculation.

In the exact calculation, we need the whole set of $A_{l,m;p,m}^{\gamma,\beta}$ for $1 \leq l, p \leq l_{max}$ and $|m| \leq l_{max}$. This can be done by a very efficient recurrence relation derived Mackowski based on the scalar addition theorem.¹³ Since we use $Y_{l,m}$ instead of P_l^m in Mackowski's original paper, we quote his results briefly in the former part of this appendix with the appropriate modification due to the different definition of $A_{l,m;p,m}^{\gamma,\beta}$. Readers should refer to the original paper for detailed derivation of his recurrence relation.

In the tight-binding calculation, each $A_{l,m;p,m}^{\gamma,\beta}$ can be calculated in terms of the Wigner 3- j symbols.³⁷ Again, the coefficients involving the Wigner 3- j symbols are efficiently obtained by the recurrence relation found by Bruning and Lo.⁹ This is briefly summarized in the latter part of this appendix.

We start with the scalar addition theorem for the axial translation from \mathbf{R}_i to \mathbf{R}_j , both of which lie on the z axis:

$$\begin{aligned} h_l^{(1)}(k_0 r_j) Y_{l,m}(\theta_j, \phi_j) & = \sum_{p=0}^{\infty} j_p(k_0 r_i) Y_{p,m}(\theta_i, \phi_i) C_{p,m;l,m}(k_0, \mathbf{R}^{ij}), \quad (\text{C1}) \end{aligned}$$

where $\mathbf{R}^{ij} = \mathbf{R}_i - \mathbf{R}_j$ is parallel or antiparallel to the z axis. It is straightforward to derive the following recurrence relation for $C_{l,m;p,m}$:

$$\begin{aligned} C_{p,m;l,m} & = \sqrt{\frac{(2l+1)(2l-1)}{(l+m)(l-m)}} \left(\sqrt{\frac{(l+m-1)(l-m-1)}{(2l-1)(2l-3)}} \right. \\ & \quad \times C_{p,m;l-2,m} + \sqrt{\frac{(p+m)(p-m)}{(2p+1)(2p-1)}} C_{p-1,m;l-1,m} \\ & \quad \left. - \sqrt{\frac{(p+m+1)(p-m+1)}{(2p+3)(2p+1)}} C_{p+1,m;l-1,m} \right), \quad (\text{C2a}) \end{aligned}$$

$$\begin{aligned} C_{p,\pm(m+1);m+1,\pm(m+1)} & = \sqrt{\frac{2m+3}{2m+2}} \left(\sqrt{\frac{(p+m+1)(p+m)}{(2p+1)(2p-1)}} C_{p-1,\pm m;m,\pm m} \right. \\ & \quad \left. + \sqrt{\frac{(p-m+1)(p-m)}{(2p+3)(2p+1)}} C_{p+1,\pm m;m,\pm m} \right). \quad (\text{C2b}) \end{aligned}$$

Note that $C_{l,m;p,m}$ vanishes when l or p is smaller than $|m|$. The initial values of $C_{p,0;0,0}$ are given by the formula

$$C_{p,0;0,0} = (-\cos \theta_{ji})^p \sqrt{2p+1} h_l^{(1)}(k_0 |\mathbf{R}^{ji}|). \quad (C3)$$

From the set of equations (C2) and (C3) we calculate $C_{p,m;l,m}$ in the following manner. First we use Eqs. (C2b) and (C3) to calculate $\{C_{p,\pm m;m,\pm m}\}$ for $0 \leq m \leq l_{max}$ and $0 \leq p \leq l_{max} + 1$. The remaining coefficients are $\{C_{p,m;l,m}\}$ for $l \geq |m|$. These are obtained by first setting $m = \pm(l-1)$ in Eq. (C2a). Then, the first term vanishes and we obtain $C_{p,\pm(l-1);l,\pm(l-1)}$. Once $C_{p,\pm(l-1);l,\pm(l-1)}$ is obtained, Eq. (C2a) successively yields the whole set of $\{C_{p,m;l,m}\}$ for $l \geq |m|$. In addition, it is easy to confirm the following symmetry properties of $C_{p,m;l,m}$:

$$\begin{aligned} C_{p,m;l,m}(k_0, \mathbf{R}^{ji}) &= (-1)^{l+p} C_{l,-m;p,-m}(k_0, \mathbf{R}^{ji}) \\ &= (-1)^{l+p} C_{p,m;l,m}(k_0, \mathbf{R}^{ij}) \\ &= C_{p,-m;l,-m}(k_0, \mathbf{R}^{ji}). \end{aligned} \quad (C4)$$

The vector addition coefficients can be immediately obtained from $C_{p,m;l,m}$. Since $A_{l,m;p,m}^{\gamma,\beta} = A_{l,m;p,m}^{\beta,\gamma}$ and $A_{l,m;p,m}^{\beta,\beta} = A_{l,m;p,m}^{\gamma,\gamma}$, we write $A_{l,m;p,m}^{\gamma,\beta}$ as follows:

$$A_{p,m;l,m}^{\gamma,\beta}(k_0, \mathbf{R}) = \begin{cases} A_{p,m;l,m}(k_0, \mathbf{R}) & \text{for } \gamma = \beta, \\ B_{p,m;l,m}(k_0, \mathbf{R}) & \text{for } \gamma \neq \beta. \end{cases} \quad (C5)$$

Then, $A_{p,m;l,m}$ and $B_{p,m;l,m}$ are given in terms of $C_{p,m;l,m}$ as

$$\begin{aligned} A_{p,m;l,m}(k_0, \mathbf{R}^{ji}) &= C_{p,m;l,m}(k_0, \mathbf{R}^{ji}) + \frac{k_0 Z_{ji}}{p+1} \sqrt{\frac{(p+m+1)(p-m+1)}{(2p+3)(2p+1)}} \\ &\quad \times C_{p+1,m;l,m}(k_0, \mathbf{R}^{ji}) + \frac{k_0 Z_{ji}}{p} \sqrt{\frac{(p+m)(p-m)}{(2p+1)(2p-1)}} \\ &\quad \times C_{p-1,m;l,m}(k_0, \mathbf{R}^{ji}), \end{aligned} \quad (C6a)$$

$$B_{p,m;l,m}(k_0, \mathbf{R}^{ji}) = ik_0 Z_{ji} \frac{m}{p(p+1)} C_{p,m;l,m}(k_0, \mathbf{R}^{ji}), \quad (C6b)$$

where Z_{ji} is the z component of \mathbf{R}^{ji} . By using the above formulas and the relation (C4) for $C_{p,m;l,m}$, we arrive at the following relations for $A_{p,m;l,m}$:

$$A_{p,m;l,m}(k_0, \mathbf{R}^{ji}) = (-1)^{l+p} A_{p,m;l,m}(k_0, \mathbf{R}^{ij}) \quad (C7a)$$

$$= (-1)^{l+p} \frac{p(p+1)}{l(l+1)} A_{l,-m;p,-m}(k_0, \mathbf{R}^{ji}) \quad (C7b)$$

$$= A_{p,-m;l,-m}(k_0, \mathbf{R}^{ji}). \quad (C7c)$$

Relations for $B_{p,m;l,m}$ are obtained by multiplying (-1) on the right-hand side of Eqs. (C7).

The coefficients $A_{p,m;l,m}$ and $B_{p,m;l,m}$ can also be obtained in terms of the Wigner 3- j symbols. For $\mathbf{R} = (0,0,Z)$ with $Z > 0$, they are given as

$$\begin{aligned} A_{p,m;l,m}(k_0, \mathbf{R}) &= (-1)^m i^{p-l} \frac{2p+1}{2p(p+1)} \sum_n (-i)^n \\ &\quad \times [l(l+1) + p(p+1) - n(n+1)] \\ &\quad \times a(m,l; -m,p;n) h_n^{(1)}(k_0 Z), \end{aligned} \quad (C8a)$$

$$\begin{aligned} B_{p,m;l,m}(k_0, \mathbf{R}) &= -2imk_0 Z (-1)^m i^{p-l} \frac{2p+1}{2p(p+1)} \\ &\quad \times \sum_n (-i)^n a(m,l; -m,p;n) h_n^{(1)}(k_0 Z). \end{aligned} \quad (C8b)$$

Here, n runs over $|l-p|, |l-p|+2, \dots, l+p$, and $a(m,l; -m,p;n)$ are given in terms of the Wigner 3- j symbol⁹ as

$$\begin{aligned} a(m,l; -m,p;n) &= (2n+1) \sqrt{\frac{(l+m)! (p-m)!}{(l-m)! (p+m)!}} \begin{pmatrix} l & p & n \\ 0 & 0 & 0 \end{pmatrix} \\ &\quad \times \begin{pmatrix} l & p & n \\ m & -m & 0 \end{pmatrix}. \end{aligned} \quad (C9)$$

According to Bruning and Lo, $a_n \equiv a(m,l; -m,p;n)$ satisfies the following recurrence relation:⁹

$$\gamma_n a_n - (\gamma_{n-1} + \gamma_{n-2} - 4m^2) a_{n-2} + \gamma_{n-3} a_{n-4} = 0, \quad (C10)$$

where γ_n is given by

$$\gamma_n = \frac{[(l+p+1)^2 - n^2][n^2 - (l-p)^2]}{4n^2 - 1}. \quad (C11)$$

The recurrence relation (C10) is obtained by setting $n=l+p+2$ and letting $a_{l+p+2} = 0$. This yields a_{l+p-2} when combined with the following expression for a_{l+p} :

$$a_{l+p} = \frac{(2l)!(2p)![(l+p)!]^2}{p!l!(p+m)!(l-m)!(2p+2l)!}. \quad (C12)$$

The successive use of Eq. (C10) gives the whole set of $\{a_n\}$ immediately.

The expression (C12) contains a factorial of very large number such as $156! \sim 10^{275}$. To evaluate the product of factorials of such large numbers it is very convenient to use the well-known theorem:

$$N! = \prod_{j=1}^{\infty} p_j^{n_j}, \quad n_j = \sum_{k=1}^{\infty} \left[\frac{N}{p_j^k} \right]. \quad (C13)$$

Here, $\{p_j\}$ are prime numbers and $[n]$ is the Gauss function, which gives the smallest integer not greater than n .

A simple estimation formula for $A_{p,m;l,m}$ and $B_{p,m;l,m}$ would be very convenient for the practical calculation of the transfer integral between modes (γ,p,m) and (β,l,m) . We give below a handy formula valid for $l,p \gg 1$ and $k_0 z < l+p$. In this case, the term of $n=l+p$ in Eqs. (C8) is the largest because $h_n^{(1)}(k_0 Z)$ is an exponentially growing function of n . Its asymptotic form is given by

$$h_n(k_0 Z) \cong -i \frac{\exp[(n+1/2)(\alpha - \tanh\alpha)]}{(n+1/2)\sqrt{\operatorname{sech}\alpha \tanh\alpha}}. \quad (\text{C14})$$

Here, α is defined by the equation $k_0 Z = (n+1/2)/\cosh\alpha$. By using the Stirling formula $N! \cong \sqrt{2\pi N} N^N e^{-N}$ for a_{l+p} in Eq. (C12), it is straightforward to derive the following formula for $A_{p,m;l,m}$ and $B_{p,m;l,m}$:

$$\begin{aligned} A_{p,m;l,m}(k_0, \mathbf{r}) &\cong -2l(-1)^{l+m} h_{l+p}^{(1)}(k_0 Z) \\ &\times \sqrt{\frac{(l+p)}{\pi(p+m)(l-m)}} \\ &\times \frac{l^l p^p}{(p+m)^{p+m}(l-m)^{l-m}}, \quad (\text{C15a}) \end{aligned}$$

$$\begin{aligned} B_{p,m;l,m}(k_0, \mathbf{r}) &\cong -2i \frac{m}{p} k_0 Z (-1)^{l+m} h_{l+p}^{(1)}(k_0 Z) \\ &\times \sqrt{\frac{(l+p)}{\pi(p+m)(l-m)}} \\ &\times \frac{l^l p^p}{(p+m)^{p+m}(l-m)^{l-m}}. \quad (\text{C15b}) \end{aligned}$$

This is called the maximum term approximation. Substitution of Eq. (C14) into (C15) yields

$$\begin{aligned} A_{p,m;l,m} &\cong i(-1)^{l+m} |A_{p,m;l,m}|, \\ B_{p,m;l,m} &\cong (-1)^{l+m+1} \operatorname{sgn}(m) |B_{p,m;l,m}|. \quad (\text{C16}) \end{aligned}$$

By using the maximum term approximation, it is easy to show that $|A_{p,m;l,m}| \gg |B_{p,m;l,m}|$ and that $|A_{p,m;l,m}|$ is a decreasing function of $|m|$.

APPENDIX D: NORMAL MODE OF THE MIE RESONANCE

The Mie resonance of a single sphere is determined by the condition $\cot\delta_l^\beta = 0$. This condition gives the resonance size parameter $S_{l,n}^\beta$. The index n denotes the radial behavior of the internal electric field. Thus, the Mie resonance is labeled by (β, l, n) . Now, the internal field is generally given as a linear combination of the VSH's $\mathbf{E}_{l,m}^\beta(j_l, kr, \theta, \phi)$. At the Mie resonance, k is given by $\sqrt{\varepsilon} S_{l,n}^\beta / a$. Here, ε and a are the dielectric constant and the radius of the sphere. Therefore, VHS is labeled by (β, l, m, n) at the Mie resonance. What is, then, the role of m ?

To clarify the role of m let us consider the incidence of a plane wave along the z axis. Appendix C shows that it has only $m = \pm 1$ components. Therefore, the internal field is given by the linear combination of $\mathbf{E}_{l,1}^\beta$ and $\mathbf{E}_{l,-1}^\beta$. The coefficients of the linear combination are determined by the symmetry relation of $c_{l,\pm 1}^\beta$. This gives the famous WG pattern.

For off-axis incidence, the plane wave has nonzero components for $m \neq \pm 1$. Therefore, the internal field is given as a sum of various VHS's. To simplify this summation we can use the symmetry relation (B4) between $a_{l,m}^\beta$ and $a_{l,-m}^\beta$. We introduce a normal field $\mathbf{F}_{l,m}^\beta$, which is a linear combination of $\mathbf{E}_{l,m}^\beta$ and $\mathbf{E}_{l,-m}^\beta$ according to the relation (B4). Note that

the normal mode depends on β , m , and the polarization of the incident light. Thus, the internal field is now given as a sum of various normal fields $\mathbf{F}_{l,m}^\beta$. They are combined so that the same WG pattern is reproduced when the incidence direction is chosen as a new z axis.

Though dependent on the nature of the incident light, the normal modes are a very convenient concept. They show that the actual degeneracy of the Mie resonance is $l+1$ because m runs from 0 through l . Other combinations of VSH's orthogonal to $\mathbf{F}_{l,m}^\beta$ are not excited. In addition, $\mathbf{F}_{l,m}^\beta$ is the observable field pattern as in the case of on-axis incidence. This is especially important for the bisphere case. The bisphere configuration gives the interaction between $\mathbf{F}_{l,m}^\beta$ of different spheres. This interaction depends on m . Therefore, the $(l+1)$ -fold degeneracy is removed. This results in a collection of peaks in the bonding and antibonding branches of the energy spectrum. Each peak, therefore, corresponds to the bonding and antibonding combinations of $\mathbf{F}_{l,m}^\beta$ in each sphere. To interpret the internal field state in the bisphere we need the characteristic field pattern of $\mathbf{F}_{l,m}^\beta$.

We are interested in the field pattern along the circumference of the sphere. Therefore, we list up in Table I the θ and ϕ dependence of each component of the normal mode $\mathbf{F}_{l,m}^\beta$. They are obtained straightforwardly from Eqs. (A1) and (B4). It should be noted that F_r is usually much larger than F_θ or F_ϕ if it exists. To draw the field pattern we also list in Table II the number of maxima for $|P_l^m|$, $|mP_l^m/\sin\theta|$, and $|\partial P_l^m/\partial\theta|$ in the range $0 \leq \theta \leq \pi$. In addition, we note that within the xy plane $P_l^m = 0$ and $mP_l^m/\sin\theta = 0$ for odd $l-m$ while $\partial P_l^m/\partial\theta = 0$ for even $l-m$. Combined use of Tables I and II gives the characteristic field pattern. Below we describe this procedure, taking the case of $\beta = N$ and xz polarized incident light as an example.

When $\beta = N$ and the polarization is within the xz plane, we have $I_{pol} + I_\beta = 2$. Therefore, $f_m^+(\phi)$ and $f_m^-(\phi)$ in Table I are, respectively, given by $2 \cos(m\phi)$ and $2i \sin(m\phi)$. Let us deal first with the case of $m=0$. In this case, the main component is F_r with a P_l dependence on θ . $|P_l|$ has $2l$ maxima along the circumference. Thus, the field patterns within the xz and yz planes are commonly given by the ringlike $2l$ spots.

Let us next consider the case of $m > 0$. Table I shows that the field pattern within the xy plane is given by $\cos m\phi$ irrespective of the values of $l-m$. Thus, we have $2m$ ringlike spots within the xy plane. The field pattern within the xz plane ($\phi=0$ or π) is dominated by F_r with a P_l^m dependence on θ . Therefore, it consists of $2(l-m+1)$ ringlike spots.

On the other hand, the field pattern within the yz plane ($\phi = \pi/2$ or $3\pi/2$) is different when m is even or odd. When m is even, $\sin m\phi$ vanishes so that the main component is F_r with P_l^m dependence on θ . Thus, the field pattern is very similar to that within the xz plane. When m is odd, F_r and F_θ vanish and F_ϕ dominates with a $mP_l^m/\sin\theta$ dependence on θ . Therefore, the field pattern is governed by the huge peaks near $\theta=0$ and π , and $2(l-m+1)$ ringlike spots lose their contrast. Other cases can be treated in the same way.

Note that when m is even the xz and yz in-plane field patterns are very similar to each other for any mode and any

polarization. This universal feature can be verified from Tables I and II.

Finally, we study the parity of the main component of the normal mode under the inversion of $z \rightarrow -z$, i.e., $\theta \rightarrow \pi - \theta$. The normal field depends on θ in three ways: P_l^m , $mP_l^m/\sin\theta$, and $\partial P_l^m/\partial\theta$. Since P_l^m satisfies $P_l^m(-x) = (-1)^{l+m}P_l^m(x)$, the parity of P_l^m and $mP_l^m/\sin\theta$ is $+1$ while $\partial P_l^m/\partial\theta$ is -1 when $l-m$ is even. In addition, r and θ components change sign with $z \rightarrow -z$ while that of ϕ re-

mains unchanged. On the basis of these facts and the identification of the main components of normal field in Table I, it is straightforward to show that the parity of the main component with $z \rightarrow -z$ is generally given by $(-1)^{l+m+1}$ except for the following three cases: (1) yz in-plane contour of TM modes with odd m for xz polarization incidence, (2) xz in-plane contour of TM modes for y polarization incidence, and (3) yz in-plane contour of TM modes with even m for y polarization incidence.

*Author to whom correspondence should be addressed. Electronic address: hmiyazak@olive.apph.tohoku.ac.jp

¹G. Mie, Ann. Phys. (Leipzig) **25**, 377 (1908).

²P. Debye, Ann. Phys. (Leipzig) **30**, 57 (1909).

³M. Born and E. Wolf, *Principles of Optics* (Pergamon Press, Oxford, 1965), p. 633.

⁴van der Hulst, *Light Scattering by Small Particles* (Dover Publications, New York, 1981).

⁵*Optical Effects Associated with Small Particles*, edited by P. W. Barber and R. K. Chang, Advanced Series in Applied Physics (World Scientific, Singapore, 1988), Vol. 1.

⁶*Confined Electrons and Photons*, edited by E. Burstein and C. Weisbush, NATO ASI Series (Plenum Press, New York, 1995), Vol. 340.

⁷Y. Kawabe, C. Spiegelberg, A. Schulzgen, M. F. Nabor, B. Kippelen, E. A. Mash, P. M. Allemand, M. Kuwata-Gonokami, K. Takeda, and N. Peyghambarian, Appl. Phys. Lett. **72**, 141 (1998); M. Kuwata-Gonokami and K. Takeda, Opt. Mater. **90**, 12 (1998).

⁸C. Linag and Y. T. Lo, Radio Sci. **2**, 1481 (1967).

⁹J. H. Bruning and Y. T. Lo, IEEE Trans. Antennas Propag. **AP-19**, 378 (1971); **AP-19**, 391 (1971).

¹⁰B. Peterson and S. Ström, Phys. Rev. D **8**, 3661 (1973).

¹¹F. Borghese, P. Denti, R. Saija, G. Toscano, and O. I. Sindoni, J. Opt. Soc. Am. A **4**, 1984 (1987).

¹²K. A. Fuller, Appl. Opt. **30**, 4716 (1991).

¹³D. W. Mackowski, Proc. R. Soc. London, Ser. A **433**, 599 (1991).

¹⁴M. Bayer, T. Gutbrod, J. P. Reithmaier, A. Forchel, T. L. Reinicke, P. A. Knipp, A. A. Dremin, and V. D. Kulakovskii, Phys. Rev. Lett. **81**, 2582 (1998).

¹⁵T. Mukaiyama, K. Takeda, H. Miyazaki, Y. Jimba, and M. Kuwata-Gonokami, Phys. Rev. Lett. **82**, 4623 (1999).

¹⁶E. Lidorikis, M. M. Sigalas, E. N. Economou, and C. M. Soukoulis, Phys. Rev. Lett. **81**, 1405 (1998).

¹⁷*Photonic Band Gaps and Localization*, edited by C. M. Soukoulis (Plenum, New York, 1993).

¹⁸J. Joannopoulos, R. D. Meada, and J. Wim, *Photonic Crystals* (Princeton University Press, Princeton, 1995).

¹⁹*Photonic Band Gap Materials*, edited by C. M. Soukoulis (Kluwer, Dordrecht, 1996).

²⁰P. M. Hui and Neil F. Johnson, in *Solid State Physics*, edited by H. Ehrenreich and F. Spaepen (Academic, New York, 1995), Vol. 49, p. 151.

²¹K. Ohtaka, H. Miyazaki, and T. Ueta, Mater. Sci. Eng., B **48**, 153 (1997).

²²H. Miyazaki and K. Ohtaka, Phys. Rev. B **58**, 6920 (1998).

²³T. Fujimura, T. Itoh, K. Hayashibe, K. Edamatsu, S. Shimoyama, R. Shimada, A. Imada, T. Koda, Y. Segawa, N. Chiba, H. Muramatsu, and T. Ataka, Mater. Sci. Eng., B **48**, 94 (1997); T. Fujimura, K. Edamatsu, T. Itoh, R. Shimada, A. Imada, T. Koda, N. Chiba, H. Muramatsu, and T. Ataka, Opt. Lett. **22**, 489 (1997).

²⁴B. Friedman and J. Russek, Q. Appl. Math. **12**, 13 (1954).

²⁵S. Stein, Q. Appl. Math. **19**, 15 (1961).

²⁶O. R. Cruzan, Q. Appl. Math. **20**, 33 (1962).

²⁷Y.-I. Xu, J. Comput. Appl. Math. **85**, 53 (1997); J. Comput. Phys. **139**, 137 (1998).

²⁸P. Chylek, J. D. Pendleton, and R. G. Pinnick, Appl. Opt. **24**, 3940 (1985).

²⁹N. W. Ashcroft and N. D. Mermin, *Solid State Physics* (Holt-Saunders International Editions, Philadelphia, 1976).

³⁰C. J. Joachain, *Quantum Collision Theory* (North-Holland, Amsterdam, 1983), p. 241.

³¹K. Ohtaka, Phys. Rev. B **19**, 5057 (1979); J. Phys. C **13**, 667 (1980).

³²A. Tip, J. Math. Phys. **38**, 3545 (1997); F. J. Garcia de Abajo and H. Howie, Phys. Rev. Lett. **80**, 5180 (1998).

³³D. S. Jones, *The Theory of Electromagnetism* (Pergamon Press, Oxford, 1964).

³⁴F. Haake, *Statistical Treatment of Open Systems by Generalized Master Equations*, Springer Tracts in Modern Physics (Springer Verlag, Berlin, 1973), Vol. 66.

³⁵J. A. Stratton, *Electromagnetic Theory* (McGraw-Hill, New York, 1941), p. 397.

³⁶Coexistence of almost localized and extended orbits reminds us of the narrow d bands and wide sp bands in transition metals. In fact, there exists a tight-binding treatment of the resonant d states based on the KKR method. This gives a powerful clue to the present problem. For review article, see D. W. Bulletin, in *Solid State Physics*, edited by H. Ehrenreich, F. Seitz, and D. Turnbull (Academic Press, New York, 1980), Vol. 35, p. 129.

³⁷A. Messiah, *Quantum Mechanics* (Wiley, New York, 1976), Vol. II.

³⁸A. B. Pippard, *Response and Stability* (Cambridge University Press, Cambridge, 1985).

³⁹*Handbook of Mathematical Functions*, edited by M. Abramowitz and I. A. Stegun (Dover, New York, 1970).

⁴⁰J. D. Jackson, *Classical Electrodynamics* (Wiley, New York, 1962).